J. Mech. Phys. Solids 145 (2020) 104168

Contents lists available at ScienceDirect

Journal of the Mechanics and Physics of Solids

journal homepage: www.elsevier.com/locate/mps

Shear induced supercritical pitchfork bifurcation of pre-buckled bands, from narrow strips to wide plates

Weicheng Huang, Yunbo Wang, Xuanhe Li, Mohammad K. Jawed *

Department of Mechanical and Aerospace Engineering, University of California, Los Angeles, CA 90095, United States

ARTICLE INFO

Keywords:
Elastic rods
Elastic plates
Numerical simulation
Buckling instability

ABSTRACT

We combine discrete differential geometry (DDG)-based models and desktop experiments to study supercritical pitchfork bifurcation of a pre-compressed elastic plate under lateral end translation, with a focus on its width effect. Based on the ratio among length, width, and thickness, the elastic structures in our study fall into three different structural categories: rods, ribbons, and plates. In order to numerically simulate the mechanical response of these structures, we employ two DDG-based numerical frameworks — Discrete Anisotropic Rods method and Discrete Elastic Plates method. Even though the multi-stability and bifurcation of a narrow strip can be precisely captured by a naive one dimensional rod model, it fails to match with experiments as the ribbon increases in width. A two dimensional approach using a plate model, on the other hand, accurately predicts the geometrically nonlinear deformations and the supercritical pitchfork points for plate even when the width is as large as half of the length. Exploiting the efficiency and robustness of the simulator, we perform a systematic parameter sweep on plate size and lateral displacement to build a phase diagram of different configurations of the elastic plates. We find that the deformed configuration of the nearly developable strips can be described, up to a very good approximation, using the bending and twisting of the centerline. This indicates that a one dimensional energy model for the simulation of nearly developable strips can potentially be developed in the future. The results can serve as a benchmark for future numerical investigations into modeling of ribbons. Our study can also provide guidelines on the choice of the appropriate structural model – rod vs. ribbon vs. plate – in simulation of thin elastic structures.

1. Introduction

Thin elastic structures, e.g., narrow rods and wide plates, can perform complex mechanical response when subjected to simple boundary conditions or moderate external forces. The behavior is in the geometrically nonlinear regime, like buckling instability, which makes these structures suitable for the design of advanced metamaterials and intelligent systems (Lestringant et al., 2019). Specifically, snapping and bifurcation, i.e. a swift transformation process between multiple phases in response to external loading, exist in both artificial and natural systems, including slap bracelet (Kebadze et al., 2004), Venus flytrap (Forterre et al., 2005), toy poppers (Pandey et al., 2014), and robotics (Chen et al., 2018). Previous investigations of snap buckling mainly focused on one dimensional rod or ribbon-like system under different loading and boundary conditions, e.g. asymmetrical constraints (Gomez et al., 2017; Sano and Wada, 2018), stretching (Starostin and van der Heijden, 2008; Morigaki et al., 2016), twisting (Sano and Wada, 2019), shearing (Yu and Hanna, 2019), and out-of-plane compression (Zhang et al., 2019; Wan et al., 2019). Even though the

* Corresponding author.
E-mail address: khalidjm@seas.ucla.edu (M.K. Jawed).

https://doi.org/10.1016/j.jmps.2020.104168
Received 16 March 2020; Received in revised form 13 July 2020; Accepted 21 September 2020
Available online 25 September 2020

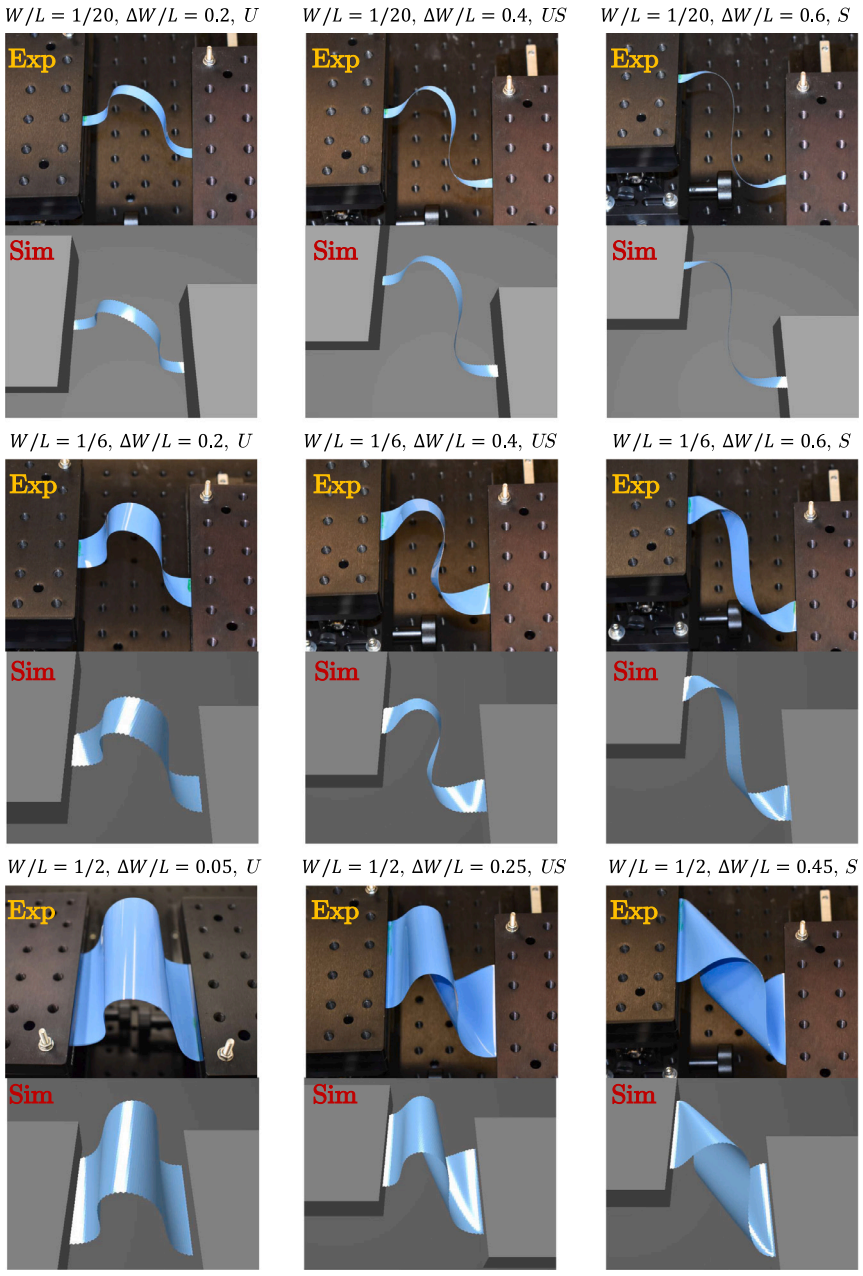

Fig. 1. Snapshots of elastic plates in different topologies (U, S, US) from both desktop experiments and numerical simulations. Here, the pre-compressed distance is $\Delta L/L = 1/2$.

buckling instability and post-buckling behavior in two dimensional curved surfaces, such as cylinder (Bende et al., 2015; Pezzulla et al., 2017; Jiang et al., 2018; Lavrenčič and Brank, 2018) and sphere/hemisphere (Huang, 1964, 1969; Lazarus et al., 2012; Shim et al., 2012; Bende et al., 2015; Marthelot et al., 2017; Evkin et al., 2017; Hutchinson and Thompson, 2018), have previously been studied, the mechanics behind the transverse shear induced bifurcation in wide strips remains uncovered, i.e. the gap between narrow strips and wide plates has not yet been systematically investigated (Yu and Hanna, 2019). This paper presents a general point of view on the shear induced bifurcations of pre-buckled plates, from narrow to wide. Here, we consider the following definitions: a rod is a one dimensional object; a ribbon is a narrow two dimensional developable surface; a plate is a two dimensional surface that allows both bending and stretching. In Fig. 1, we provide some snapshots of elastic plates in different topologies from both desktop experiments and numerical simulations. We start with a narrow strip (length $L \gg$ width $W \gg$ thickness b), then gradually increase its width that satisfies $L \sim W \gg b$ to reveal the relations between one dimensional anisotropic Kirchhoff rod model and

two dimensional Föppl–von Kármán plate equations, for a fundamental understanding of the mechanics of a class of thin elastic structures.

A straightforward approach to study the narrow strip is by a one dimensional Kirchhoff rod model (Yu and Hanna, 2019), and there are much prior investigations on Kirchhoff equations, e.g. Antman (Antman and Kenney, 1981; Antman and Jordan, 1975), Maddocks (Kehrbaum and Maddocks, 1999), Nizette and Goriely (Nizette and Goriely, 1999), and Ameline et al. (Ameline et al., 2017). Moreover, previous analytical, numerical, and experimental studies showed different deformed configurations of one dimensional rod-like structures in both isotropic cross section (Van der Heijden and Thompson, 2000; Van der Heijden et al., 2003; Goyal et al., 2005) and anisotropic cross section (Van der Heijden and Thompson, 1998; Yu and Hanna, 2019; Sano and Wada, 2019; Xu et al., 2019). However, a strip with developable surface assumption would behave fundamentally differently compared with a naive rod model (Starostin and Van Der Heijden, 2007). Sadowsky first derived an one dimensional energy functional for a narrow ribbon ($L \gg W \gg b$) (Sadowsky, 1930), and his work was later generalized by Wunderlich to account for finite width (Wunderlich, 1962). Their dimensional reduction was made possible by focusing on developable configurations of the ribbon, which are preferred energetically in the thin width limit. Developable surfaces are special cases of ruled surfaces, i.e. they are spanned by a set of straight lines called generatrices or rulings: the one dimensional elastic energy functional in Wunderlich's formulation is based on a reconstruction of the surface of the ribbon in terms of its centerline, and of the angle between the generatrices and the centerline tangent (Dias and Audoly, 2015). Next, the equilibrium problem of ribbon structures can be solved by principle of virtual work and variational method. Starostin and van der Heijden found the equilibrium equations for naturally flat rectangular ribbons (Starostin and Van Der Heijden, 2007), and later extended to helical shapes (Starostin and van der Heijden, 2008). Dias et al. summarized developable ribbon model into a generalized energy functional, with the consideration of non-zero curvatures in both out-of-plane and in-plane (geodesic) directions, such that the same model can describe both a rectangular ribbon and an annular ribbon (Dias and Audoly, 2015). Their analytical work treated the ribbon as a special case of a thin rod, with an internal parameter and kinematic constraints, and these specificities could be incorporated naturally into the classical theory of thin rods (Audoly and Pomeau, 2010). Next, they extended the smooth ribbon model into a folded case by introducing a ridge angle, and two different models – centerline model and ridge model – were later proposed to investigate the buckling instability and post-buckling behaviors of folded annular strips (Dias et al., 2012; Dias and Audoly, 2014). However, all these investigations are under the assumption that the surface is developable, such that the stretching energy is forbidden during the deformed process. A two dimensional approach, on the other hand, allows the stretching strain in the middle surface of plate, and is preferred when studying the typology of Möbius strip (Kleiman et al., 2016) and patterns in helical ribbon (Ghafouri and Bruinsma, 2005; Guo et al., 2014; Armon et al., 2014), whose stretching energies are no longer trivial compared with bending energies.

One the other side, directly solving the ordinary differential equations (ODEs) or partial differential equations (PDEs) from the results of functional variation is not easy and, when geometric nonlinearity is involved, requires resource intensive computation. Usually, Finite Element Method (FEM) is preferred by the computational mechanics community to investigate the mechanical response in solids and structures (Wood and Zienkiewicz, 1977; Bonet and Wood, 1997; Zienkiewicz and Taylor, 2005; Hughes, 2012; De Borst et al., 2012; Liu et al., 2019). Recently, another type of numerical frameworks – Discrete Differential Geometry (DDG) based methods – are becoming more and more popular in the computer graphics community, due to its computational efficiency. Previous DDG-based numerical frameworks showed surprisingly successful performance in simulating thin elastic structures, e.g. rods (Grégoire and Schömer, 2007; Spillmann and Teschner, 2008a; Bergou et al., 2008, 2010; Audoly and Pomeau, 2010; Audoly et al., 2013; Lazarus et al., 2013; Jawed et al., 2014; Li et al., 2019, 2020), ribbons (Shen et al., 2015), plates/shells (Baraff and Witkin, 1998; House and Breen, 2000; Grinspun et al., 2002, 2003; Choi and Ko, 2005; Bridson et al., 2005; Wardetzky et al., 2007; Batty et al., 2012), and gridshells/cosserat nets (Spillmann and Teschner, 2008b; Pérez et al., 2015; Baek et al., 2018; Baek and Reis, 2019; Panetta et al., 2019; Qin et al., 2020). Sano and Wada (2019) studied the width effect on the twist-induced snapping of elastic strips, from isotropic rods to anisotropic ribbons, by considering a width related regularization parameter; however, they mainly focused on the transitions between isotropic rods to anisotropic narrow ribbons, i.e. the structure they considered is within scope of $L \gg W \sim b$, and their method may fail to capture the growth from narrow ribbons to plates, $L \sim W \gg b$. Numerical frameworks on elastic strip with finite width focused on the Wunderlich model (Starostin and Van Der Heijden, 2007; Starostin and van der Heijden, 2008; Giomi and Mahadevan, 2010; Audoly and Seffen, 2016; Starostin and van der Heijden, 2015; Dias and Audoly, 2015; Shen et al., 2015; Moore and Healey, 2015), while the solutions have to be manually divided into several phases to avoid the issues at inflection points (Starostin and van der Heijden, 2015; Yu and Hanna, 2019). Also, the log barrier term in one dimensional ribbon energy functional would cause numerical issues and, therefore, Moore and Healey (2015) introduced an elliptic regularization parameter to avoid numerical difficulties. However, the final result would unavoidably be somewhat influenced by the choice of the regularization parameter. More recently, Charrondière et al. implemented a discrete simulation of the Wunderlich model using novel curvature-based elements and successfully captured the deformation of ribbons in a number of examples, e.g. equilibrium shapes of naturally helical ribbons under gravity (Charrondière et al., 2020).

Here, we combine tabletop experiments with DDG-based simulations to study the effect of width on the mechanical response of a pre-compressed (i.e. longitudinally displaced) elastic plates under lateral displacement (i.e. transverse shear). We aim to quantify the transition of the mechanics of these plates from a rod-like behavior to a plate-like response, as the width increases. Toward that end, we employ two DDG-based numerical frameworks: Discrete Anisotropic Rods (DAR) that simulates a rod based on the deformation of the one-dimensional centerline and Discrete Elastic Plates (DEP) that models the two-dimensional plate. Specifically, the DEP model is derived from Seung and Nelson (1988), Liang and Mahadevan (2009), and Savin et al. (2011). In DEP, the continuous plate is discretized into multiple equilateral-triangular elements, with stretching energies associated with each edge and bending energies associated with two neighboring triangles. This type of discrete representation of thin plate has been proved to converge

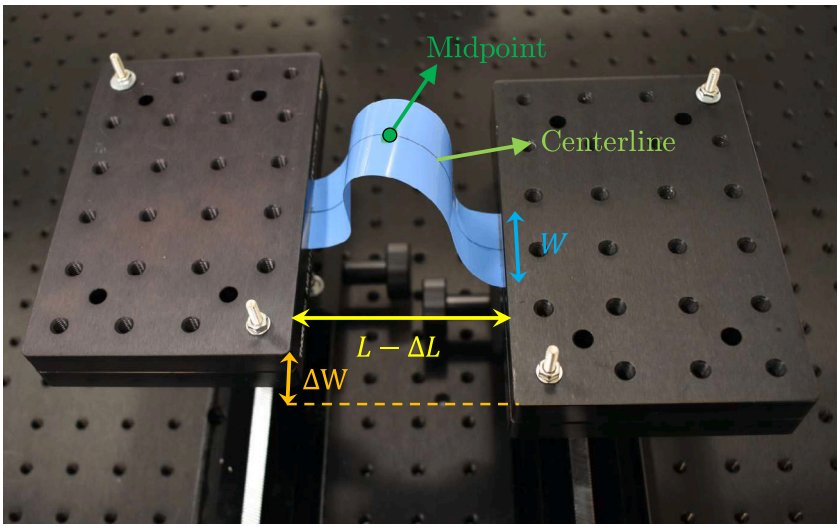

Fig. 2. Experimental setup. A rectangular plate of width W and length L is symmetrically clamped. The longitude compression is ΔL and the transverse displacement is ΔW.

to the continuum limit of Föppl–von Kármán equations (Seung and Nelson, 1988) and successfully captured the growth of gut (Savin et al., 2011) and configurations of long leaf (Liang and Mahadevan, 2009). Side by side with simulations, we record the deformation of a number of plates of varying widths under prescribed longitudinal displacement and transverse shear. Longitudinal displacement is first applied to buckle the plates and this pre-buckled plate is then subjected to lateral displacement (i.e. transverse shear), resulting in a number of qualitatively distinct deformed shapes. Excellent agreement is found between DEP simulations and desktop experiments. A systematic parameter sweep is performed on plate size and transverse shear to build a phase diagram of different shapes of elastic plates; we find the threshold shear at supercritical pitchfork point show a decreasing trend as the plates become wider. This helps us quantify the width effect on elastic plates and can serve as a benchmark for any numerical tool at the confluence of rods and plates, e.g. ribbons. In order to understand when the strip behaves like a rod vs. a plate, we use DAR to model anisotropic Kirchhoff rods and show that DAR and DEP solutions match, i.e. the strip behaves like a rod, when the width to length ratio is $\sim 1/20$. Moreover, we demonstrate that a plate with finite width can be represented by the deformation of its centerline (Ghafouri and Bruinsma, 2005), which may instigate further research into a general one-dimensional ribbon model without the assumption of developable surface. In addition to the rod and plate simulations, we also implement a discrete Sadowsky model for narrow developable ribbon. Interestingly, in our numerical framework based on balance of forces at each degree of freedom, the Sadowsky model does not capture the shear induced supercritical pitchfork in the pre-stressed narrow ribbons. However, both one dimensional rod model and two dimensional plate simulation can give reasonable predictions compared with experimental observations. However, the Sadowsky model does give a reasonable prediction if an initial solution is provided, where this initial solution can be obtained from the rod or plate simulation. Not so surprisingly, we observe that the curvatures computed by the Sadowsky model are discontinuous at the inflection points where the bending curvatures are zero.

Our contributions are as follows: We quantify the mechanical response of pre-compressed elastic plates of varying width under transverse shear. The transition between rod-like behavior to plate-like behavior is also quantified using experiments and simulations. We perform systematic quantitative validation of the DEP method using tabletop experiments. Lastly, our study points to a one-dimensional energy model for undevelopable strips that is physically accurate even when the width to length is the same order of magnitude as the length.

This paper is organized as follows: In Section 2, we introduce the geometry of our problem and describe the experimental setup. Then, in Section 3, we present the two DDG-based numerical frameworks — DAR for rods and DEP for plates. Next, results from experiments and numerical simulations are compared in Section 4. Finally, concluding remarks and avenues for future research are presented in Section 5. We also discuss the numerical issues associated with existing ribbon models in Appendix A.

2. Experimental setup

In Fig. 2, we show the experimental setup and boundary conditions used in the current study. The setup is similar to a recently published study (Yu and Hanna, 2019). The span between two slide rails is fixed at $L - \Delta L = 75$ mm for convenience, where $L \in \{100, 150\}$ mm is the length of the plates and ΔL is the transverse displacement to pre-compress the structure. The inclined angle of clamped end is a constant, $\psi = 0.0°$. The plates were cut from polyester shim stock (Artus Corp., Englewood, NJ) with a thickness of $b = 0.127 \pm 0.013$ mm (Yu and Hanna, 2019), such that the length to thickness ratio is $L/b \in \{787, 1181\}$. A variety of specimens were prepared with different lengths and widths such that $\Delta L/L \in \{1/2, 1/4\}$ and $W/L \in \{1/2, 1/3, 1/6, 1/12, 1/20\}$.

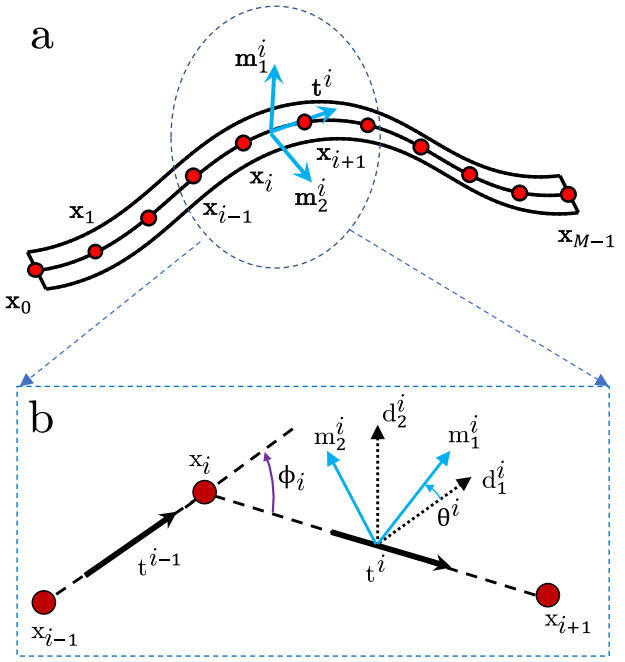

Fig. 3. (a) Discrete schematic diagram of a narrow strip. (b) Notations used in our discrete model. Bending curvature is related to turning angle, ϕ_i.

In the anisotropic rod model, we describe the plate in terms of its centerline, which is most suitable for narrow strip, while quite distinct from the description of wide plate — a surface in two dimension. The height of structural midpoint, marked as green dot in Fig. 2, is used to quantify the deformed configurations in elastic strip. The experimental data point is extracted using ImageJ, a Java-based image processing program. A strip with finite width has a shear limit that imposes an upper bound on the lateral displacement, $\Delta W_{\max}$, as discussed in Appendix B. As a result, we maintain $\Delta W \in [0, \Delta W_{\max}]$ in both experiments and simulations to avoid damage to the plates as well as numerical convergence issues. Since this is a geometry dependent problem, the material parameter (Young's modulus) does not play any role. In our simulations, the Young's modulus was set to $E = 100$ GPa.

3. Numerical model

In this section, we first discuss the one dimensional approach – DAR method – for the simulation of narrow strips approximated as an anisotropic rod. This is followed by an introduction to a two dimensional DDG-based framework – DEP method – for the simulation of elastic plates.

3.1. Discrete Anisotropic Rods (DAR) method

DAR is a special case of Discrete Elastic Rods (DER) model (Bergou et al., 2008, 2010; Jawed et al., 2018) with a noncircular cross section and two different elastic bending stiffness values along two directions of bending. As shown schematically in Fig. 3(a), the centerline of the structure is discretized into M nodes: $[\mathbf{x}_0, \ldots, \mathbf{x}_{M-1}]$, which correspond to $M-1$ edge vectors: $\mathbf{e}^0, \ldots, \mathbf{e}^{M-2}$, such that $\mathbf{e}^i = \mathbf{x}_{i+1} - \mathbf{x}_i$ and $i = 0, \ldots, M-2$. Hereafter, we use subscripts to denote quantities associated with the nodes, e.g. $\mathbf{x}_i$, and superscripts when associated with edges, e.g. $\mathbf{e}^i$. Each edge, $\mathbf{e}^i$, has an orthonormal reference frame $\{\mathbf{d}_1^i, \mathbf{d}_2^i, \mathbf{t}^i\}$ and a material frame $\{\mathbf{m}_1^i, \mathbf{m}_2^i, \mathbf{t}^i\}$. Both the frames share the tangent $\mathbf{t}^i = \mathbf{e}^i/\|\mathbf{e}^i\|$ as one of the directors, i.e. the frames remain adapted to the centerline. The first material director, $\mathbf{m}_1^i$, is the surface normal of elastic plate, and $\mathbf{m}_2^i = \mathbf{t}^i \times \mathbf{m}_1^i$. At each time step of the time marching scheme (discussed later in this section), the reference frame is updated through parallel transport in time (Jawed et al., 2018). Referring to Fig. 3(b), the material frame at the ith edge can be obtained from the reference frame using a scalar twist angle θ^i. This implies that the rod centerline can be represented using a $4M-1$ sized ($3M$ for the nodal coordinates and $M-1$ for twist angles) degree of freedom vector,

$$\mathbf{q}^{\text{rod}} = [\mathbf{x}_0, \theta^0, \mathbf{x}_1, \theta^1, \ldots \theta^{M-2}, \mathbf{x}_{M-1}]. \tag{1}$$

Based on this kinematic representation, in the remainder of this section, we discuss the formulation of elastic strains, energies, and the time stepping procedure of the DAR algorithm.

The strains of a deformed Kirchhoff's rod are comprised of three parts: stretching, bending, and twisting. Stretching strain associated with the ith edge, $\mathbf{e}^i$, is

$$\epsilon^i = \frac{\|\mathbf{e}^i\|}{\|\bar{\mathbf{e}}^i\|} - 1. \tag{2}$$

Hereafter, quantities with an overbar indicate evaluation in the undeformed state, e.g. $\|\bar{\mathbf{e}}^i\|$ is the undeformed length of the ith edge. Bending strain is captured by the curvature binormal which measures the misalignment between two consecutive edges at a node $\mathbf{x}_i$,

$$(\boldsymbol{\kappa b})_i = \frac{2\mathbf{e}^{i-1} \times \mathbf{e}^i}{\|\mathbf{e}^{i-1}\|\|\mathbf{e}^i\| + \mathbf{e}^{i-1} \cdot \mathbf{e}^i}, \tag{3}$$

its norm is $\|(\boldsymbol{\kappa b})_i\| = 2\tan\left(\phi_i/2\right)$, and ϕ_i is the angle between two consecutive edges (see Fig. 3(b)). The material curvatures are given by the inner products between the curvature binormal and material frame vectors,

$$\kappa_i^{(1)} = \frac{1}{2}\left(\mathbf{m}_2^{i-1} + \mathbf{m}_2^i\right) \cdot (\boldsymbol{\kappa b})_i, \tag{4a}$$

$$\kappa_i^{(2)} = -\frac{1}{2}\left(\mathbf{m}_1^{i-1} + \mathbf{m}_1^i\right) \cdot (\boldsymbol{\kappa b})_i. \tag{4b}$$

The twisting strain at the ith node, in the discrete setting of DER, is measured using the discrete twist

$$\tau_i = \theta^i - \theta^{i-1} + m_i^{\text{ref}}, \tag{5}$$

where m_i^{ref} is the reference twist associated with the reference frame (Bergou et al., 2008).

An elastic anisotropic rod is treated as a mass–spring system, with a lumped mass (and angular mass) at each node (and edge), and associated discrete energies, (Bergou et al., 2008, 2010)

$$E_{\text{s}}^{\text{rod}} = \frac{1}{2}\sum_{i=0}^{M-2} EA(\epsilon^i)^2\|\bar{\mathbf{e}}^i\| \tag{6a}$$

$$E_{\text{b}}^{\text{rod}} = \frac{1}{2}\sum_{i=0}^{M-1} \frac{1}{\Delta l_i}\left[EI_1(\kappa_i^{(1)} - \bar{\kappa}_i^{(1)})^2 + EI_2(\kappa_i^{(2)} - \bar{\kappa}_i^{(2)})^2\right] \tag{6b}$$

$$E_{\text{t}}^{\text{rod}} = \frac{1}{2}\sum_{i=0}^{M-1} \frac{GJ}{\Delta l_i}(\tau_i)^2, \tag{6c}$$

where A is the area of cross-section, I_1 (and I_2) are the area moments of inertia for bending along $\mathbf{m}_2^i$ (and $\mathbf{m}_1^i$), J is the polar moment of inertia, $\Delta l_i = \left(\|\mathbf{e}^i\| + \|\mathbf{e}^{i+1}\|\right)/2$ is its Voronoi length. For an elastic plate with anisotropic cross section, $EI_1 \gg EI_2$, and, as a result, its geodesic curvature remains almost unchanged and bending around the surface normal is energetically unfavorable, i.e. $\kappa_i^{(1)} \approx \bar{\kappa}_i^{(1)}$. Note that EI_1 resembles a Lagrange multiplier.

We use a first order, implicit Euler time marching scheme to numerically integrate the equations of motion from time step t_k to $t_{k+1} = t_k + h$ (h is the time step size) (Huang and Jawed, 2019),

$$\mathbb{M}\Delta\mathbf{q}_{k+1}^{\text{rod}} - h\mathbb{M}\dot{\mathbf{q}}_k^{\text{rod}} - h^2\left[(\mathbf{F}_{k+1}^{\text{int}})^{\text{rod}} + (\mathbf{F}_{k+1}^{\text{ext}})^{\text{rod}}\right] = \mathbf{0} \tag{7a}$$

$$\mathbf{q}_{k+1}^{\text{rod}} = \mathbf{q}_k^{\text{rod}} + \Delta\mathbf{q}_{k+1}^{\text{rod}} \tag{7b}$$

$$\dot{\mathbf{q}}_{k+1}^{\text{rod}} = \frac{\mathbf{q}_{k+1}^{\text{rod}} - \mathbf{q}_k^{\text{rod}}}{h}, \tag{7c}$$

where

$$(\mathbf{F}^{\text{int}})^{\text{rod}} = -\frac{\partial}{\partial\mathbf{q}^{\text{rod}}}\left(E_{\text{s}}^{\text{rod}} + E_{\text{b}}^{\text{rod}} + E_{\text{t}}^{\text{rod}}\right) \tag{8}$$

is the internal elastic force, $(\mathbf{F}^{\text{ext}})^{\text{rod}}$ is the external force vector (e.g. gravity or damping force), $\mathbb{M}$ is the diagonal mass matrix comprised of the lumped masses, and the subscript $k+1$ (and k) denotes evaluation of the quantities at time t_{k+1} (and t_k). The Jacobian associated with Eq. (7a) is necessary for Newton's iteration and can be expressed as

$$\mathbb{J} = \mathbb{M} - h^2\left[-\frac{\partial^2\left(E_s^{\text{rod}} + E_b^{\text{rod}} + E_t^{\text{rod}}\right)}{\partial\mathbf{q}^{\text{rod}}\partial\mathbf{q}^{\text{rod}}} + \frac{\partial(\mathbf{F}^{\text{ext}})^{\text{rod}}}{\partial\mathbf{q}^{\text{rod}}}\right], \tag{9}$$

where the energies and the external force are evaluated at $t = t_{k+1}$. Importantly, as long as the gradient matrix of the external force $\left(\frac{\partial(\mathbf{F}^{\text{ext}})^{\text{rod}}}{\partial\mathbf{q}^{\text{rod}}}\right)$ is banded (e.g. gravity and viscous damping), the Jacobian $\mathbb{J}$ is a banded matrix and the time complexity of this algorithm is $O(n)$, i.e. the computational time scales linearly with the number of nodes (Bergou et al., 2010). This computational efficiency has motivated its application in the animation industry (e.g. hair simulation for movies) as well as its adoption in mechanical engineering.

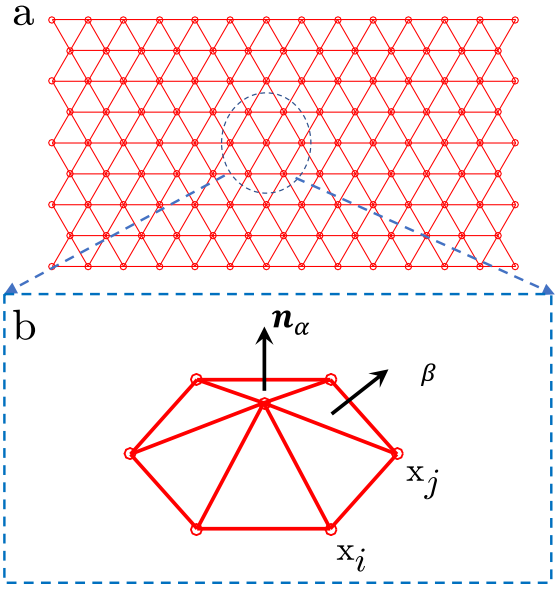

Fig. 4. (a) Discretization of a two dimensional plate. (b) Notations used in discrete elastic plate model. Surface normal of αth equilateral triangle mesh is $\mathbf{n}_\alpha$.

3.2. Discrete Elastic Plates (DEP) method

Next, we introduce a DDG-based simulation of two dimensional elastic plate. Similar to the previous anisotropic rod model, we treat the elastic plate as a mass–spring system, with lumped masses at the vertices. A discrete elastic energy is associated with each vertex. In Fig. 4(a), the two dimensional plate is discretized into N nodes and N_{mesh} equilateral triangular faces, such that the degree of freedom vector has a size of $3N$,

$$\mathbf{q}^{\text{plate}} = \left[\mathbf{x}_0, \mathbf{x}_1, \dots, \mathbf{x}_{N-1}\right]. \tag{10}$$

The total potential in two dimensional plate is the sum of the elastic stretching and bending energies (Savin et al., 2011),

$$E_{\text{s}}^{\text{plate}} = \frac{\sqrt{3}}{4} Eb \sum_{ij}^{N_{\text{edge}}} \left(\|\mathbf{e}^{ij}\| - \|\bar{\mathbf{e}}^{ij}\|\right)^2 \tag{11a}$$

$$E_{\text{b}}^{\text{plate}} = \frac{1}{\sqrt{3}} \frac{Eb^3}{12} \sum_{\alpha\beta}^{N_{\text{pair}}} \left(\mathbf{n}_\alpha - \mathbf{n}_\beta\right)^2, \tag{11b}$$

where b is the plate thickness, $\mathbf{e}^{ij} = \mathbf{x}_i - \mathbf{x}_j$ is the edge vector between ith and jth nodes, $\|\bar{\mathbf{e}}^{ij}\|$ is its undeformed length, N_{edge} is the total edge number in discrete plate model, N_{pair} is the total bending pairs of discrete plate (a bending pair is comprised of two neighboring triangular faces), and $\mathbf{n}_\alpha$ (and $\mathbf{n}_\beta$) is the surface normal of the α-th (and β-th) triangular face, as shown in Fig. 4(b). This discrete representation of the energy functional presented above has been shown to converge to the continuum limit of Föppl–von Kármán equations used to describe the nonlinear mechanics of thin plates (Seung and Nelson, 1988; Liang and Mahadevan, 2009; Savin et al., 2011). The time marching scheme in elastic plate model is similar to the rod simulation, i.e. the equations of motion from time step t_k to $t_{k+1} = t_k + h$ (h is the time step size) is obtained through implicit Euler approach, and $(\mathbf{F}^{\text{int}})^{\text{plate}} = -\frac{\partial}{\partial \mathbf{q}^{\text{plate}}}(E_{\text{s}}^{\text{plate}} + E_{\text{b}}^{\text{plate}})$ is the internal elastic force vector in plate model. The Jacobian matrix of plate simulation is sparse but non-banded, and, as such, we cannot achieve $O(N)$ time complexity. The difference in computation between rod vs. plate simulation becomes more and more significant as the number of nodes increases. Naturally, whenever possible, a rod model is favorable over a plate model.

4. Results

In this section, we study the shear induced bifurcations of pre-buckled plates. We present the numerical results from both anisotropic rod model and plate model, and compare them with experimental data. We use $M = 100$ nodes for rod simulation and $N_{\text{mesh}} \approx 2000$ in plate model. A convergence study on the number of nodes is presented in Appendix C. In one dimensional rod model, 14 DOFs, $\left[\mathbf{x}_0, \theta^0, \mathbf{x}_1, \mathbf{x}_{M-2}, \theta^{M-2}, \mathbf{x}_{M-1}\right]$, are constrained. These DOFs correspond to the location, tangent, and rotation at two ends; this boundary condition emulates the clamped boundary at two ends. All other nodes and edges are free to evolve based on the balance of forces. For plate simulation, the nodes in the first two and last two "columns" are constrained to impose an equivalent clamped boundary condition. We briefly review the Euler buckling of elastic strip and then discuss in detail the shear

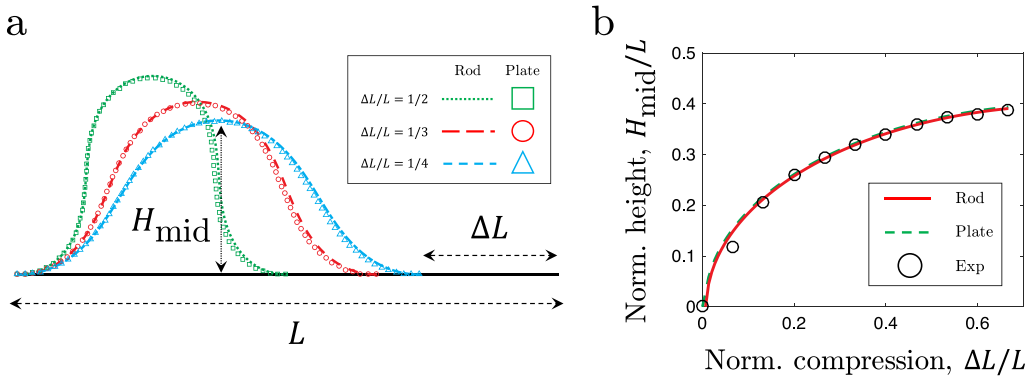

Fig. 5. (a) Pre-buckled configurations of elastic strips obtained from (i) rod model (line) and (ii) plate model (symbolic). (b) normalized midpoint height, H_{mid}/L, as a function of actuated distance, $\Delta L/L$, from (i) rod simulation, (ii) plate simulation, and (iii) experimental data.

induced bifurcations of the pre-buckled plate, from narrow to wide. The influence of gravity on these systems is generally weak and negligible (Yu and Hanna, 2019), such that we keep gravity out of our frameworks. However, the effect of gravity can be easily accounted for in the discrete model as an external force.

4.1. Pre-buckled configurations in elastic plate

The thin elastic strip would undergo buckling instability when the uniaxial compressive force exceeds a threshold; this has been studied since the days of the elastica theory of Euler in the 18th century. We review the buckled configuration of an elastic strip, and compare the simulation results from rod (DAR) and plate (DEP) models with experimental data.

Referring to the solid black line in Fig. 5(a), we consider a strip of length L along the x-axis. The arclength parameter of the centerline is $s \in [0, L]$. One end at $s = 0$ is fixed, and the another extremity at $s = L$ is longitudinally displaced, i.e. compressed, from $x = L$ to $x = L - \Delta L$ to induce buckling. Due to inextensibility of thin elastic strip, its midpoint height, H_{mid}, is independent of the material properties and only related to the compressive distance ΔL, i.e. the system can be described by a naive geometric model. In simulations, the compression speed of clamped end is set to be $\Delta v_L = 1$ mm/ s to ensure quasistatic response of the structure (Jawed et al., 2014; Baek et al., 2018) and avoid higher order modes of dynamic buckling (Audoly and Neukirch, 2005; Ji and Waas, 2008; Vandenberghe and Villermaux, 2013; Heisser et al., 2018). In Fig. 5(a), we show the deformed configurations of elastic strips at different actuated distances, $\Delta L/L \in \{1/2, 1/3, 1/4\}$, from both one dimensional rod model (line) and two dimensional plate simulation (symbols). A good agreement can be found between rod and plate models, as the transverse direction (width effect) of elastic strip does not matter in this simple case of out-of-plane deformation. In Fig. 5(b), for a quantitative comparison between experiments and simulations, we measure the normalized midpoint height, H_{mid}/L, as a function of the normalized compressive distance, $\Delta L/L$, from (i) rod model; (ii) plate model; and (iii) experimental data. A good match indicates the accuracy of our presented discrete models in the planar buckling case, which is a prerequisite for further investigations into 3D scenarios involving shear induced bifurcations of pre-buckled strips.

4.2. Shear induced bifurcations of pre-stressed plate

With the numerical frameworks and pre-buckled elastic strip constructed beforehand, we now turn to the main contribution of the current study and systematically investigate its supercritical pitchfork under lateral end translations. In both experiments and simulations (Fig. 1), we found that the pre-stressed U shaped strips first transitions into US configuration after the supercritical pitchfork point, next shifts to S patterns when transverse shear goes beyond the second threshold. Regarding the nomenclature of the patterns, we follow Yu and Hanna (Yu and Hanna, 2019). The same authors studied, using experiments and theory, the bifurcation phenomenon at the first critical translation point and reported two symmetric US ($US+$ and $US-$) patterns that later transform into S ($S+$ and $S-$) patterns (Yu and Hanna, 2019). Here, as the main focus is the width effect of elastic strips, we only briefly discuss the bifurcation phenomenon in Appendix D and demonstrate that DEP model can successfully reproduce all the patterns observed in experiments.

We first quantitatively study the shear induced bifurcations of elastic plates at a pre-compression parameter of $\Delta L/L = 1/2$. Similar to the previous trial, the transverse speed in both the rod and plate simulations is set to be $\Delta v_W = 1$mm/s to ensure quasistatic response of structures. In Fig. 6, we present the evolution of the normalized midpoint height, H_{mid}/L, with the normalized transverse shear, $\Delta W/L$, at different length to width ratio, $W/L \in \{1/20, 1/12, 1/6, 1/2\}$, of the plates. When the strip is narrow, e.g. $W/L = 1/20$ in Fig. 6(a), the difference between anisotropic rod model and plate framework is small, and both of them match well with experimental data. The U shaped configuration of narrow strip first goes into US configuration at $\Delta W_1/L \approx 0.36$, next transitions to S pattern after $\Delta W_2/L \approx 0.52$. These observations match previous experimental observations on extremely narrow plates, $W/L = 1/80$ (Yu and Hanna, 2019). As the width of the plate increases, e.g. $W/L = 1/12$ in Fig. 6(b), the critical values of

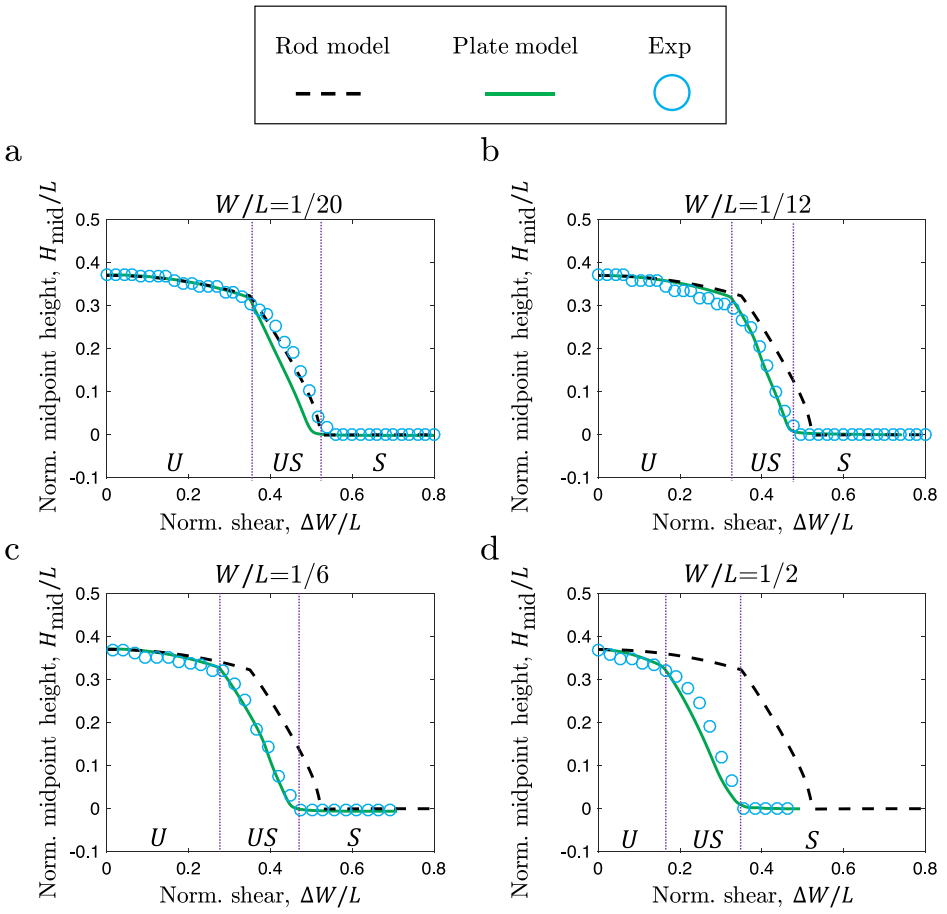

Fig. 6. Relations between normalized midpoint height, H_{mid}/L, and normalized transverse shear, $\Delta W/L$, for plates with different width, $W/L \in \{1/20, 1/12, 1/6, 1/2\}$. Here the pre-compressed distance is $\Delta L/L = 1/2$.

$\Delta W/L$ at the two critical points decrease. The plate simulation matches well with experiments, while the rod model starts to show deviation from the experimental data. Nonetheless, the difference is still trivial and, given the computational efficiency of DAR, it can be the preferred simulation tool in practice at this W/L ratio. Noteworthy is the performance of the simple Kirchhoff rod model in simulating structures ($W \gg b, L \sim 10W$) that are physically different from a rod.

Width effects start to appear as the width is increased beyond $W/L = 1/12$ in Figs. 6(c–d). For plates with larger length to width ratio, $W/L \in \{1/6, 1/2\}$, the first critical threshold drops to approximately $\Delta W_1/L = 0.27$ and $\Delta W_1/L = 0.17$. In this regime, the rod simulations cannot give accurate predictions; the two dimensional plate framework, on the other hand, successfully captures the shifts of critical points with the width in elastic strips. Even though the supercritical pitchfork points might not be obvious in the plot of geometric quantities in Fig. 6, they are noticeable in the load–displacement curves in Appendix E (Fig. E.18).

The transitions between US pattern and S pattern exhibit a similar trend where the second threshold values, $\Delta W_2/L$, decreases with increasing width. This threshold value can be easily obtained from the plots of H_{mid}/L vs. $\Delta W/L$ in Fig. 6. Beyond this second critical point, the midpoint height of the plate remains almost unchanged with normalized shear. Representative configurations from experiments and simulations are provided in Fig. 1.

We next turn to another pre-stressed state of elastic plate at a lower value of the longitudinal displacement with $\Delta L/L = 1/4$. We again focus on the critical points for the transition from a rod-like to a plate-like behavior of the elastic plates. In Fig. 7, we present the evolution of the normalized midpoint height, H_{mid}/L, with the normalized transverse shear, $\Delta W/L$, at different values of length to width ratio, $W/L \in \{1/20, 1/12, 1/6, 1/2\}$. The first and second critical points for the narrow strip ($W/L = 1/20$, Fig. 7(a)) are $\Delta W_1/L = 0.23$ and $\Delta W_2/L = 0.37$, which are lower than the case of $\Delta L/L = 1/2$. As the width of the plate is increases in Figs. 7(b–d), the rod model starts to deviate from the plate simulation and experiments. The critical shear distance at which the plate transitions from U to US decreases by $15.8\%, 29.1\%$, and 65.6% (compared with the case of $W/L = 1/20$) as the width increases ($W/L \in \{1/12, 1/6, 1/2\}$). A similar trend is noted for the boundaries between US pattern and S pattern. Again, excellent agreement between plate simulations and experimental data is found in all cases, while the rod model overestimates the critical points ($\Delta W_1/L$ and $\Delta W_2/L$) when the plates are not narrow enough.

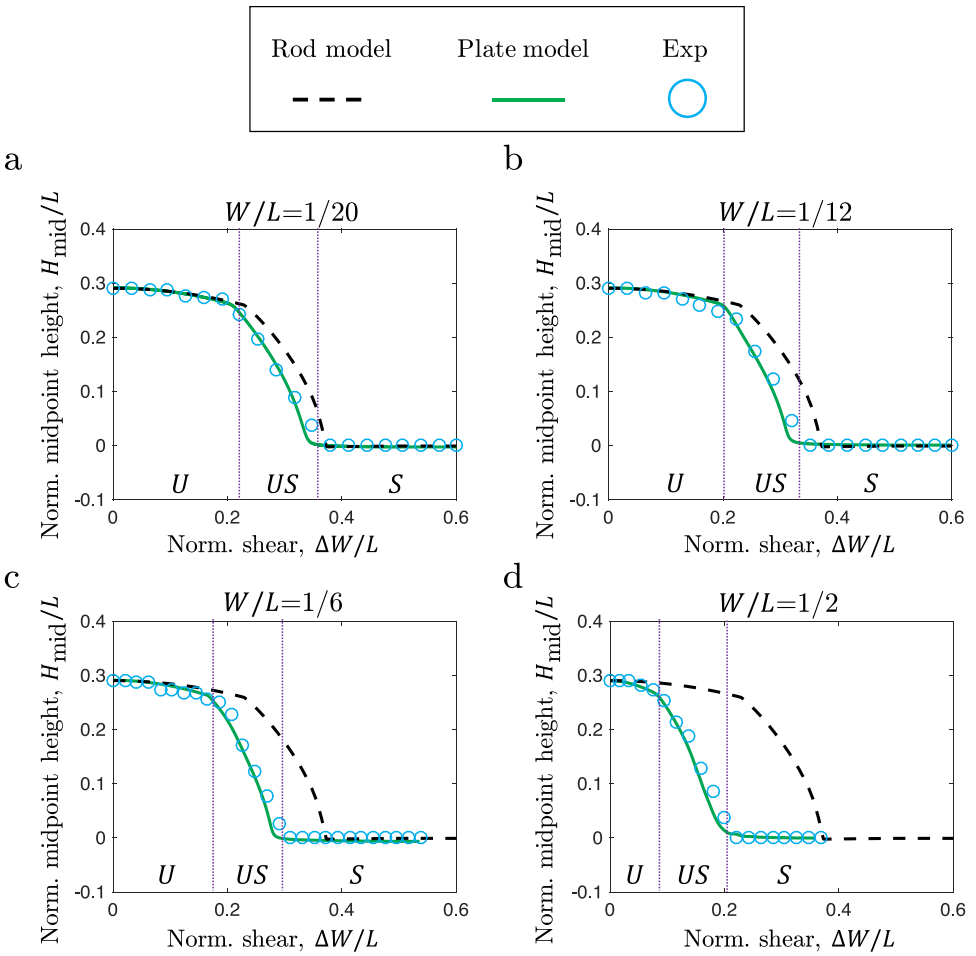

Fig. 7. Relations between normalized midpoint height, H_{mid}/L, and normalized transverse shear, $\Delta W/L$, for plate with different width, $W/L \in \{1/20, 1/12, 1/6, 1/2\}$. The pre-compressed distance is $\Delta L/L = 1/4$.

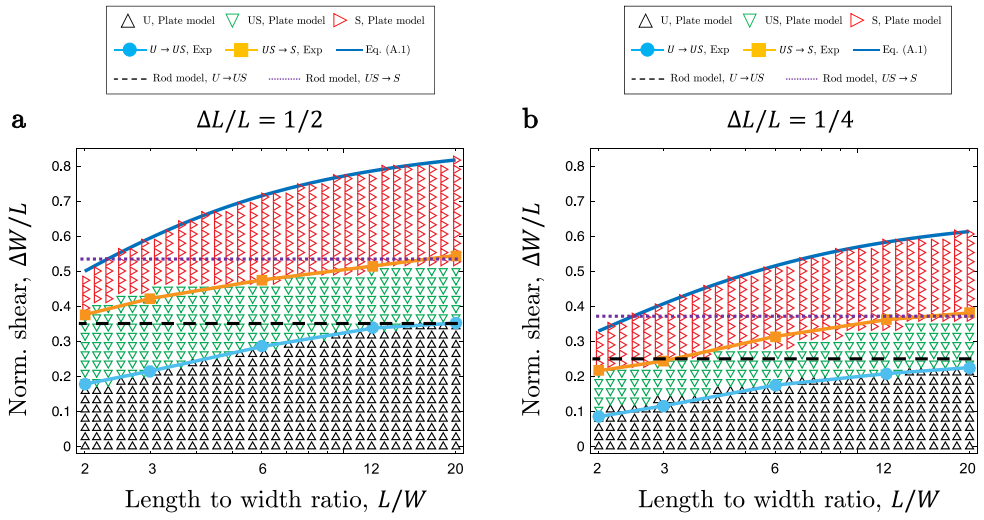

Fig. 8. Phase diagrams of shear-induced deformed configurations in pre-buckled plates. (a) $\Delta L/L = 1/2$ and (b) $\Delta L/L = 1/4$.

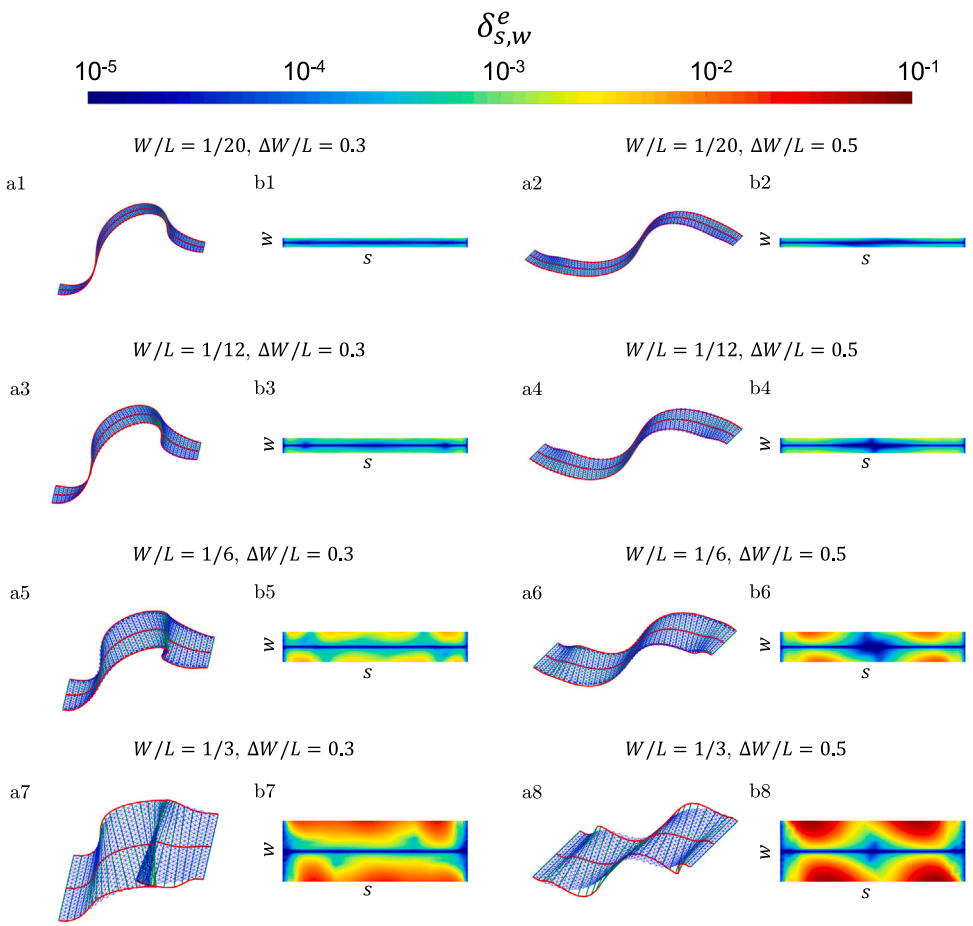

Fig. 9. (a) Deformed configurations of plates with different length to width ratio and transverse shear evaluated from DEP simulations (blue triangular mesh) and centerline-based renderings (red lines). (b) Relative errors between plate simulations and centerline-based data. (For interpretation of the references to color in this figure legend, the reader is referred to the web version of this article.)

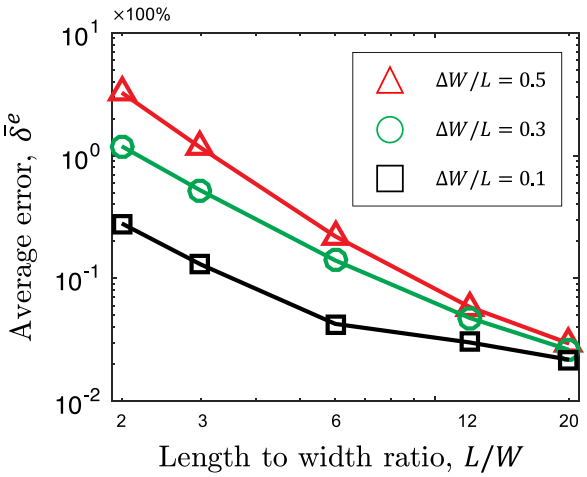

Fig. 10. The relative errors between plate model and centerline-based data as a function plate size.

Exploiting the efficiency and robustness of DDG-based simulators, in Fig. 8, we perform a two dimensional parameter sweep, by varying both length to width ratio, $L/W \in [2, 20]$, and normalized transverse shear, $\Delta W/L \in \left[0, \Delta W_{\max}/L\right]$, to show the phase

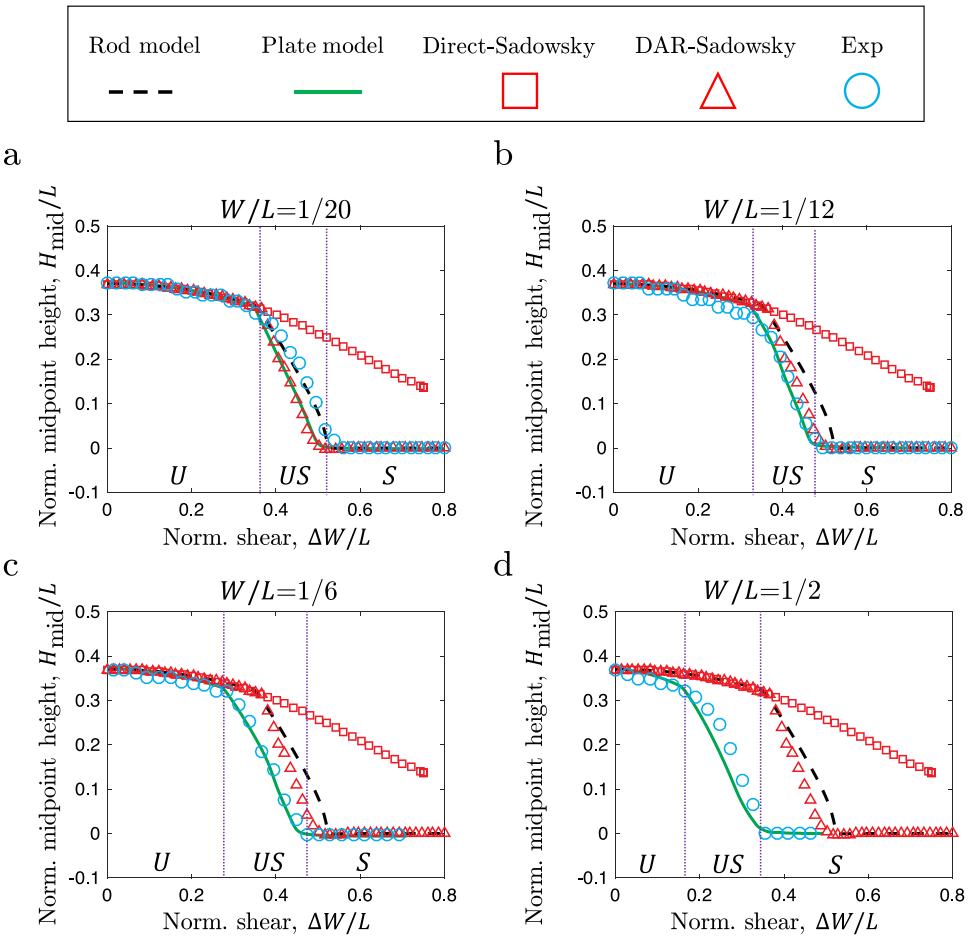

Fig. A.11. Normalized midpoint height, H_{mid}/L as a function of normalized transverse shear, $\Delta W/L$, from anisotropic rod model, plate model, and two Sadowsky models. Here the pre-compressed distance is $\Delta L/L = 1/2$.

diagrams of the elastic plates with two specific pre-buckled configurations, $\Delta L/L = 1/2$ (in Fig. 8(a)) and $\Delta L/L = 1/4$ (in Fig. 8(b)). Both first and second thresholds show an increasing trend as the width of the plate decreases. The boundaries in the phase diagram show good agreement between plate model and experiment. However, the predictions from anisotropic rod model remain unchanged and the phase boundaries from rod model in Fig. 8 are horizontal lines. Rod-based model is no longer reliable as the width of the plate grows, which emphasizes the width effect of elastic strip under transverse shear and the need of two dimensional plate approach. Also, as expected, the threshold boundaries (along $\Delta W/L$) in $\Delta L/L = 1/4$ are lower than the ones in $\Delta L/L = 1/2$.

4.3. Towards one-dimensional ribbon model

Here, we demonstrate that the deformation of an elastic strip with finite width can be reasonably represented only by the deformation of its centerline, e.g. the bending, twisting, and stretching of a single framed curve. In Fig. 9(a), we plot the deformed strips with different size, $W/L \in \{1/20, 1/12, 1/6, 1/3\}$, and normalized transverse shear, $\Delta W/L \in \{0.3, 0.5\}$, from plate simulation (triangular mesh). The same figure also shows the configurations of the centerline (solid red line) that best approximates the deformed shape of the strip. In the following, we compare the topology of the structure from the centerline-based approximation with the actual configuration from plate simulation (remarks on ribbon-based model are included in Appendix F).

In this centerline-based approximation, each node can be represented using its location in (s, w) space, where $s \in [0, 1]$ is the normalized arc-length parameter and $w \in [-W/2, W/2]$ denotes the position along the width. Upon dividing the centerline into a number of nodes, the kth node on the centerline, with $s = s_k$, can be used to make an approximation for the deformed position of any node on the plate with $s = s_k$ and $w \in [-W/2, W/2]$:

$$\mathbf{x}^c_{k,w} = \mathbf{x}^p_k + w\frac{(\bar{\mathbf{m}}^k_2 + \bar{\mathbf{m}}^{k-1}_2)}{2}, \tag{12}$$

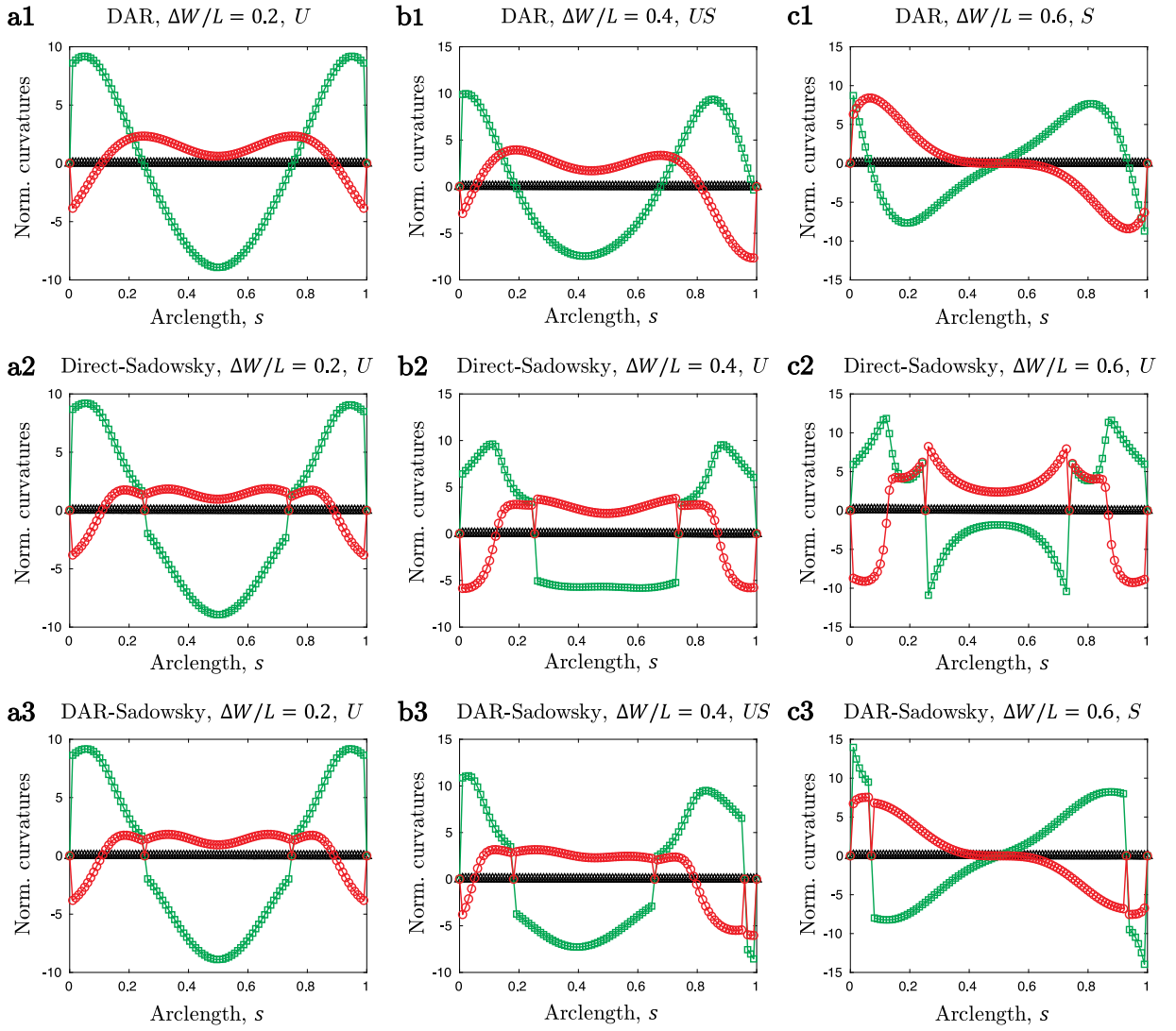

Fig. A.12. Normalized bending curvatures and twisting curvatures vary along strip arclength for (a1-c1) DAR; (a2–c2) direct-Sadowsky model; and (a3–c3) DAR-Sadowsky model. The green square is bending curvature $\kappa^{(2)}L$, the red dot is twisting curvature τL, and the black triangular is the geodesic (in-plane) curvature $\kappa^{(1)}$ L.

where $\mathbf{x}^c_{k,w}$ is the location of a node in (s_k, w), $\mathbf{x}^p_k$ is the location of the kth node on the centerline, and $\bar{\mathbf{m}}^k_2 = \bar{\mathbf{t}}^k \times \bar{\mathbf{m}}^k_1$ is the second material director on the edge vector between $s = s_{k+1}$ and $s = s_k$ (see Fig. 3), $\bar{\mathbf{t}}^k$ is the tangent vector on the same edge, and $\bar{\mathbf{m}}^k_1$ is first material director, i.e. the surface normal. In other words, each node is related to the configuration of the centerline by only three curvature quantities. Here, the surface normal $\bar{\mathbf{m}}^k_1$ is obtained from the normal vector of triangular mesh on plate centerline; the second material director is then simply $\bar{\mathbf{m}}^k_2 = \bar{\mathbf{t}}^k \times \bar{\mathbf{m}}^k_1$. We use an overbar to differentiate between the material frames from plate data and the ones in anisotropic rod model. In Fig. 9(b), we show the relative error, $\delta^e_{s,w}$, along the plate surface described by (s, w), where

$$\delta^e_{s,w} = \frac{\|\mathbf{x}^c_{k,w} - \mathbf{x}^p_{k,w}\|}{L} \tag{13}$$

is evaluated based on the distance between the deformed positions of the nodes obtained from the centerline-based approximation in Eq. (12) and the direct solution of the DEP simulation, $\mathbf{x}^p_{k,w}$. In all different cases described in Fig. 9, the relative error increases from the centerline ($w = 0$) towards the edge and from the clamped ends to the middle. The maximum errors occur close to the conical areas, details of conical areas can be found in Fig. B.15. The relative error remains within the tolerance $\lesssim 2\%$ when the strips are narrow, e.g. $W/L \leq 1/6$; while a significant deviation can be observed for a wide strip undergoing large transverse shear in Fig. 10. In order to summarize the error from centerline-based approximation in Fig. 10, we show the average error, $\bar{\delta}^e = \sum^N \delta^e_{s,w}/N$ (here N is the total number of nodes in plate simulation) as a function length to width ratio, $L/W \in \{2, 3, 6, 12, 20\}$ at different values

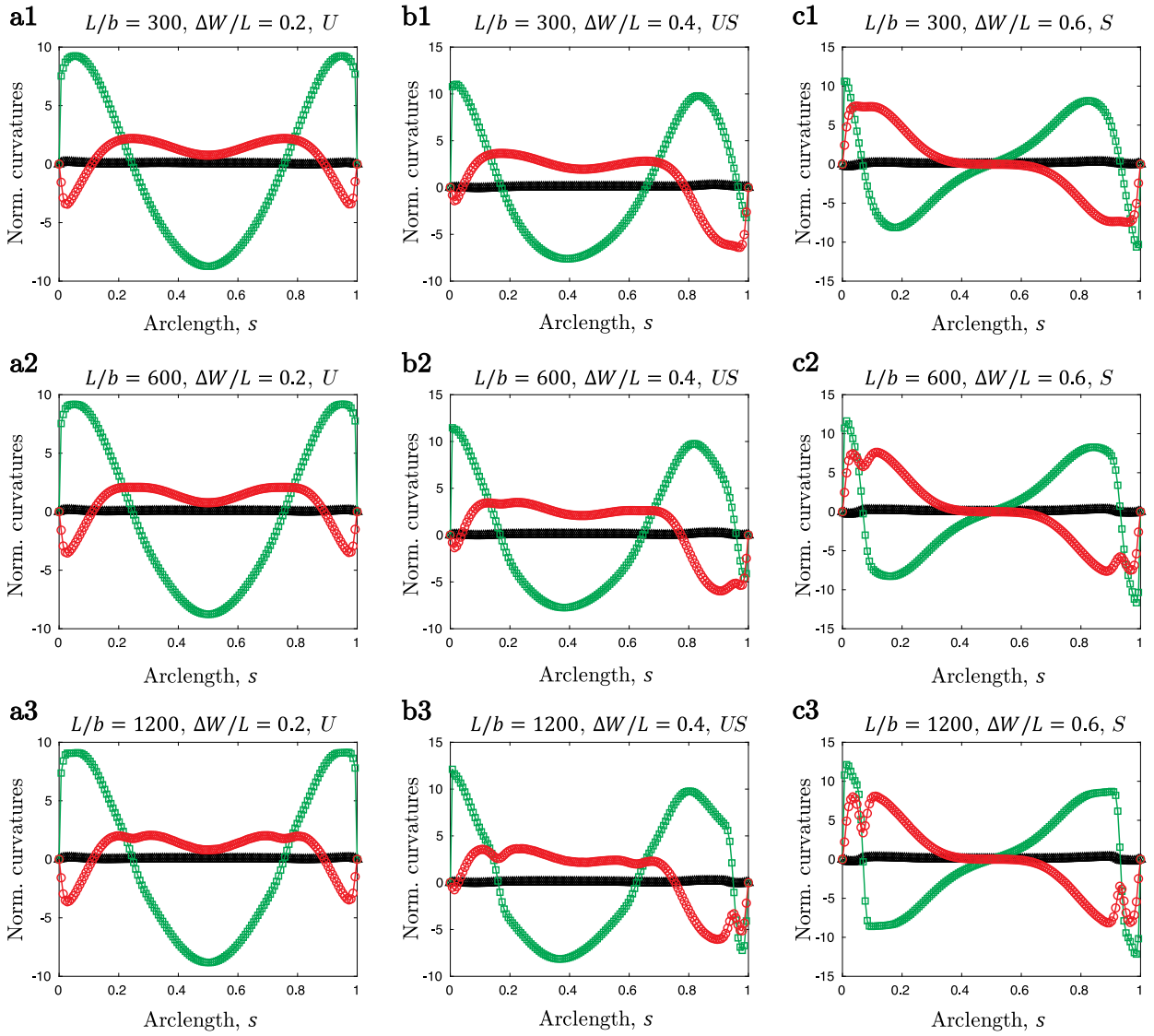

Fig. A.13. Normalized bending curvatures and twisting curvatures vary along narrow plate centerline for different thickness $L/b \in \{300, 600, 1200\}$. Here the width to length ratio is $W/L = 1/20$. The green square is bending curvature $\kappa^{(2)}L$, the red dot is twisting curvature τL, and the black triangular is the geodesic (in-plane) curvature $\kappa^{(1)}L$.

of transverse displacement, $\Delta W/L \in \{0.1, 0.3, 0.5\}$. This indicates that the centerline-based approximation is reasonable as long as $L/W > 6$ or $\Delta W/L < 0.3$. Moreover, since the DEP framework can readily gives us the energy as a function of the deformation of the centerline, empirical fitting (e.g. using a neural network) can potentially be used to obtain a one-dimensional energy model for undevelopable ribbons. This model can serve as a benchmark for future analytical energy models.

5. Conclusion

We studied supercritical pitchfork and bifurcations of elastic plates with finite width subject to compression, shear, and symmetric clamping. For this purpose, two discrete different geometry (DDG)-based numerical frameworks – one dimensional Discrete Anisotropic Rods (DAR) model and two dimensional Discrete Elastic Plates (DEP) framework – were introduced in the current work to systematically study the width effect of pre-buckled plates under lateral end translations. We found that, the one dimensional Kirchhoff equations for perfectly anisotropic rods serve as a good guide to the behavior of narrow plates, while fails to give the accurate predictions as the width increases. The two dimensional approach, on the other hand, matches well with experimental observations for both narrow strips and wide plates. The critical points, as well as maximum transverse translations, showed a decreasing trend as the strip goes from narrow to wide; this raised the need for a two dimensional approach, instead of a

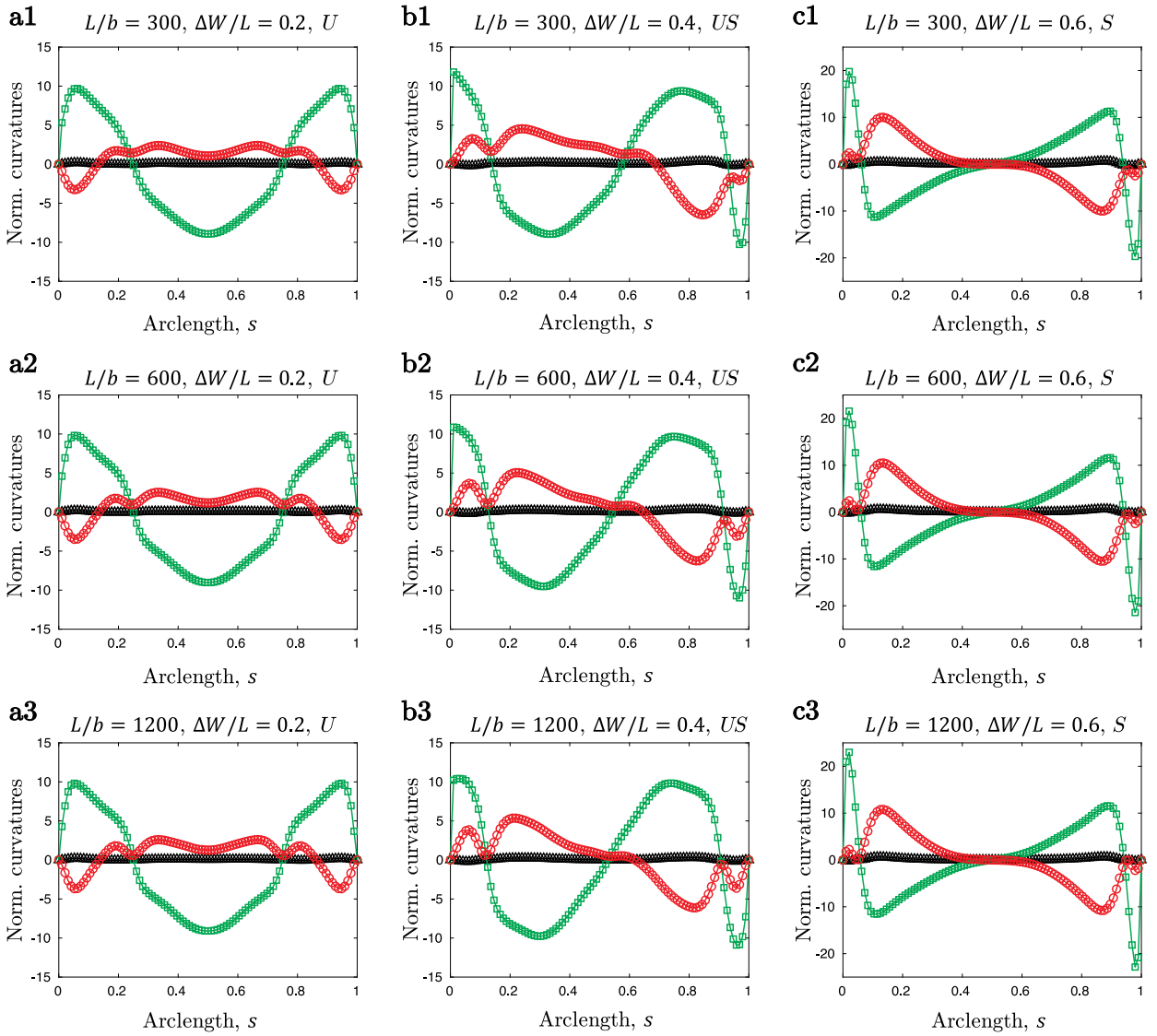

Fig. A.14. Normalized bending curvatures and twisting curvatures vary along wide plate centerline for different thickness $L/b \in \{300, 600, 1200\}$. Here the width to length ratio is $W/L = 1/6$. The green square is bending curvature $\kappa^{(2)}L$, the red dot is twisting curvature τL, and the black triangular is the geodesic (in-plane) curvature $\kappa^{(1)}L$.

one-dimensional Kirchhoff rod model, for investigation of elastic strips. We hope our findings could inspire the design of advanced structural systems and functional metamaterials, e.g. provide guidelines to avoid the instability in engineering settings.

Moreover, this unifying view bridges the gap between different types of reduced models, i.e. from classical Kirchhoff rod theory, to narrow ribbon model, and finally to the theory of elastic plate, for a fundamental understanding of thin elastic structures. The limitations in existing ribbon models that often fail at the inflection points or necessitate choice of regularization parameters (details in Appendix A) can be avoided by the presented two dimensional approach. Exploiting the efficiency and robustness of DDG-based numerical simulator, it would also be interesting to find a data-driven approach for the simulation of ribbon with undevelopable surface, i.e. using the numerical data from the general two dimensional plate model to train a neural network as a one-dimensional energy model for simulation of ribbon-like structures.

CRediT authorship contribution statement

Weicheng Huang: Conceptualization, Methodology, Software, Validation, Investigation, Writing - original draft, Visualization. **Yunbo Wang:** Methodology, Validation. **Xuanhe Li:** Methodology, Validation. **Mohammad K. Jawed:** Conceptualization, Writing - review & editing, Supervision, Project administration, Funding acquisition.

Declaration of competing interest

The authors declare that they have no known competing financial interests or personal relationships that could have appeared to influence the work reported in this paper.

Acknowledgments

We acknowledge support from the National Science Foundation, United States (Award # IIS-1925360) and the Henry Samueli School of Engineering and Applied Science, University of California, Los Angeles, United States. We thank Dr. Tian Yu for useful discussion.

Appendix A. Issues in existing ribbon model

In this section, we discuss the issues in the existing one dimensional developable ribbon model. First, the original Kirchhoff elastic energy of a naturally straight inextensible rod, E^{rod}, is given by (Audoly and Pomeau, 2010)

$$E^{\text{rod}} = \int_0^L \left[EI_1(\kappa^{(1)})^2 + EI_2(\kappa^{(2)})^2 + GJ(\tau)^2\right] ds, \tag{A.1}$$

where $\kappa^{(1)}$ and $\kappa^{(2)}$ are the bending curvatures, τ is the twisting curvature, $EI_1 = E\frac{1}{12}bW^3$ and $EI_2 = E\frac{1}{12}Wb^3$ are the bending moduli of the two principal directions of the cross section, and $GJ = \frac{E}{2(1+\nu)}\frac{1}{3}Wb^3$ is the twist modulus. Note that we can easily replace $GJ = 2EI_2$ when $\nu = 0$. The effect of Poisson ratio is in Appendix G. For the narrow strip with anisotropic cross section, e.g. $EI_1 \gg EI_2$, the in-plane curvature is the geodesic curvature and remains unchanged, $\kappa^{(1)} \equiv \bar{\kappa}^{(1)}$, which is the case of the anisotropic rod model discussed in this paper.

The one dimensional strip model proposed by Starostin and van der Heijden (2015) treated the ribbon structure as a developable surface and considered its width effect,

$$E_1^{\text{ribbon}} = \int_0^L E\frac{1}{12}Wb^3 \left\{ \left[\kappa^{(2)}(1+\eta^2)\right]^2 \frac{1}{W\eta'} \log\left(\frac{1+W\eta'/2}{1-W\eta'/2}\right)\right\} ds, \tag{A.2}$$

where $\eta = \tau/\kappa^{(2)}$. However, the solution of Eq. (A.2) is partitioned into multiple pieces by inflection points, such that we need to manually tune the simulations for desired results (see Appendix E of Ref. (Yu and Hanna, 2019) as a reference). Also, the log barrier energy function in Eq. (A.2) would be infinite at the conical zones, resulting numerical singularities in discrete model.

In Ref. (Moore and Healey, 2015), Moore and Healey introduced an elliptic regularization parameter to the energy functional (see Eq. (89) of their original paper),

$$E_2^{\text{ribbon}} = \int_0^L E\frac{1}{12}Wb^3 \left\{ \left[\kappa^{(2)}(1+\eta^2)\right]^2 \frac{1}{W\eta'} \log\left(\frac{1+W\eta'/2}{1-W\eta'/2}\right)\right\} ds + \int_0^L \frac{1}{2}K(\eta')^2 ds \tag{A.3}$$

to avoid the numerical difficulties, where the stiffness K performs like a stiff spring to prevent η' from going beyond a threshold so that the log term in Eq. (A.2) is far away from zero. The final results, obviously, would be sensitive to the choice of regularized parameter K (Moore and Healey, 2015). If K is small, the simulator would still meet numerical issues; if K is large, the results would not be acceptable.

For the developable ribbon with small width, $L \gg W$, the Wunderlich's energy functional reduces to Sadowsky's limit (Sadowsky, 1930),

$$E_3^{\text{ribbon}} = \int_0^L EI_2 \left[(\kappa^{(2)})^2 + 2(\tau)^2 + \frac{(\tau)^4}{(\kappa^{(2)})^2}\right] ds. \tag{A.4}$$

To avoid numerical singularity and allow the stretching of strip mid-surface during the bending and twisting deformations, Sano and Wada (2019) introduced a width-depended regularized parameter to the denominator of Eq. (A.4), such that the one dimensional energy functional of elastic rod with anisotropic cross section can be obtained by

$$E_4^{\text{ribbon}} = \int_0^L \left[EI_1(\kappa^{(1)})^2 + EI_2(\kappa^{(2)})^2 + GJ(\tau)^2\right] ds + \int_0^L EI_2 \left[\frac{(\tau)^4}{1/\zeta^2 + (\kappa^{(2)})^2}\right] ds, \tag{A.5}$$

where $\zeta^2 = (1-\nu)W^4/60b^2$, W is the width of the cross section, b is its thickness, and ν is the Poisson ratio, which has insensitive influence on structural response (Sano and Wada, 2019). The formulation has been used in a study on the twist-induced snapping in a bent elastic rod and ribbon (Sano and Wada, 2019). However, this one dimensional energy formulation fails to capture the width effect of elastic strip addressed in our study. In Ref. Sano and Wada (2019), they considered a structure with $L \gg W \sim b$, e.g. the longitudinal dimension is much larger than the width and thickness, and cross section is "weakly" anisotropic, from circular to elliptical then to the ribbon with small width to thickness ratio.

We first implement the Sadowsky model in a discrete format by simply replacing the bending and twisting of a rod in Eq. (A.1) by the Sadowsky's energy in Eq. (A.5)). As expected, we found the final results show no variation with ζ when ζ is large enough, and we set ζ to be 10^8. In Fig. A.11, we plot the numerical results from anisotropic rod model (Eq. (A.1)), plate simulation, and Sadowsky model (Eq. (A.5)) at different values of normalized width, W/L (cf. Fig. 6). Here, the pre-stressed distance is $\Delta L/L = 1/2$. In our

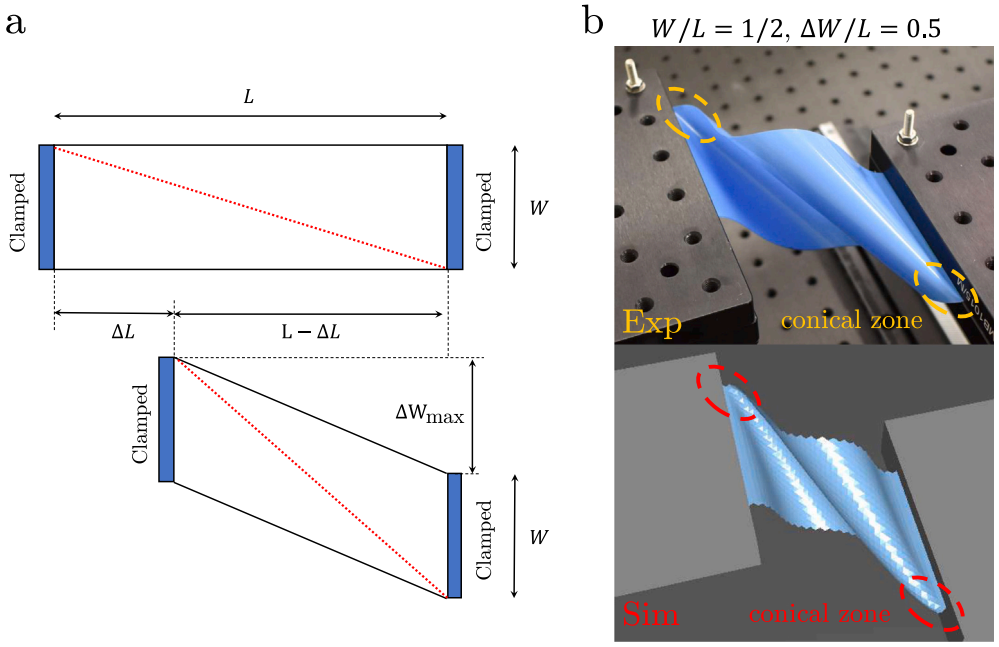

Fig. B.15. (a) Schematic diagram of the shear limit in S pattern. (b) Configurations of plate under maximum transverse shear, $W/L = 1/2, \Delta L/L = 1/2, \Delta W/L = 1/2$, from desktop experiment and numerical simulation.

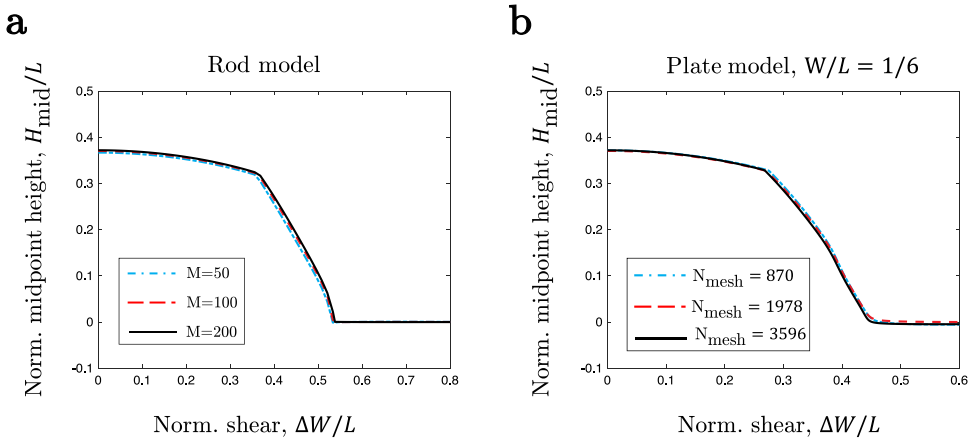

Fig. C.16. Convergence study for (a) rod model and (b) plate model.

simulations, we start with $\Delta W/L = 0$ and slowly increase the shear displacement. This "Direct-Sadowsky" model fails to capture the supercritical pitchfork point at $\Delta W/L = 0.36$ in Fig. A.11(a) that was predicted by both rod model and plate simulations. This is because the Sadowsky model holds the developable surface assumption, i.e. the twisting curvature has to be zero where the bending curvature changes its direction. This assumption is too "rigid" to transition from U to US pattern. To overcome the energy barrier in the Sadowsky model at the inflection points, we implement the "DAR-Sadowsky" simulation, where the initial configuration of the structure is obtained from rod-based simulations and the Sadowsky model is then used to find the equilibrium configuration. Referring to Fig. A.11, the DAR-Sadowsky model can reasonably capture the experimental observations. However, unlike the plate model, it cannot capture the dependence on width.

Next, to better describe the issues at the inflection point, we plot the bending and twisting curvatures of the centerline in Fig. A.12, from (i) DAR, (ii) Direct-Sadowsky, and (iii) DAR-Sadowsky. The curvatures predicted by rod model are smooth everywhere, while the curvatures in the Direct-Sadowsky and DAR-Sadowsky models are discontinuous at the inflection points when the bending curvature changes direction. Unsurprisingly, the number of inflection point does not change in the Direct-Sadowsky model owing to the energy barrier and the strip is always in U patterns.

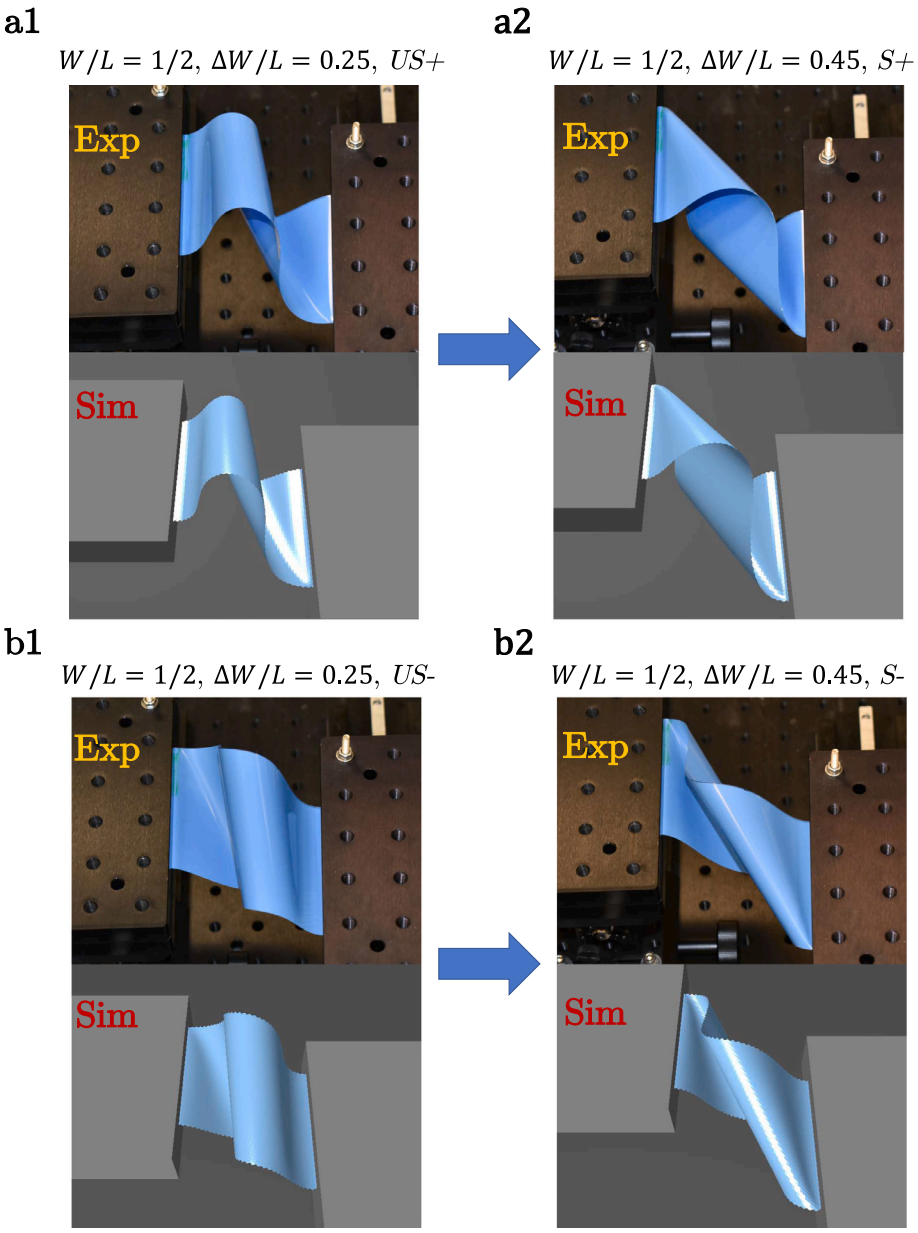

Fig. D.17. Bifurcations in US patterns and S patterns from desktop experiments and discrete plate simulations. (a1) $US+$ configuration; (a2) $S+$ configuration; (b1) $US-$ configuration; (b2) $S-$ configuration.

Finally, we turn to the plate model to better understand the curvatures at the inflection points. In Fig. A.13, we plot the centerline curvatures along the arclength of a narrow plate ($W/L = 1/20$), with different thickness: (1) $L/b = 300$, (2) $L/b = 600$, and (c) $L/b = 1200$. At a relatively large plate thickness ($L/b = 300$), the twisting curvatures are smooth at the inflection points. As the plate becomes thinner, the twisting curvatures show hints of discontinuity when the bending curvature changes the direction. Keep in mind that stretching is energetically more expensive as the thickness decreases and the surface becomes more and more developable.

This effect of thickness is more obvious in Fig. A.14 that shows the same data as Fig. A.13 but for a wider plate with $W/L = 1/6$. Here, the twisting curvatures at the inflection points become closer and closer to zero as the plate thickness decreases and the surfaces become more and more inextensible. Qualitatively speaking, the extreme case with zero thickness is the assumption behind the Sadowsky and Wunderlich models. For an ideal ribbon model (Sadowsky and Wunderlich models) with developable assumption, the stretching is totally forbidden, such that the curvature are discontinuous and, in our numerical framework, such model cannot capture the supercritical pitchfork. On the other hand, the two dimensional Föppl–von Kármán (FvK) plate model allows a small but nonzero stretching at the inflection points, and successfully captures the transition between U and US patterns.

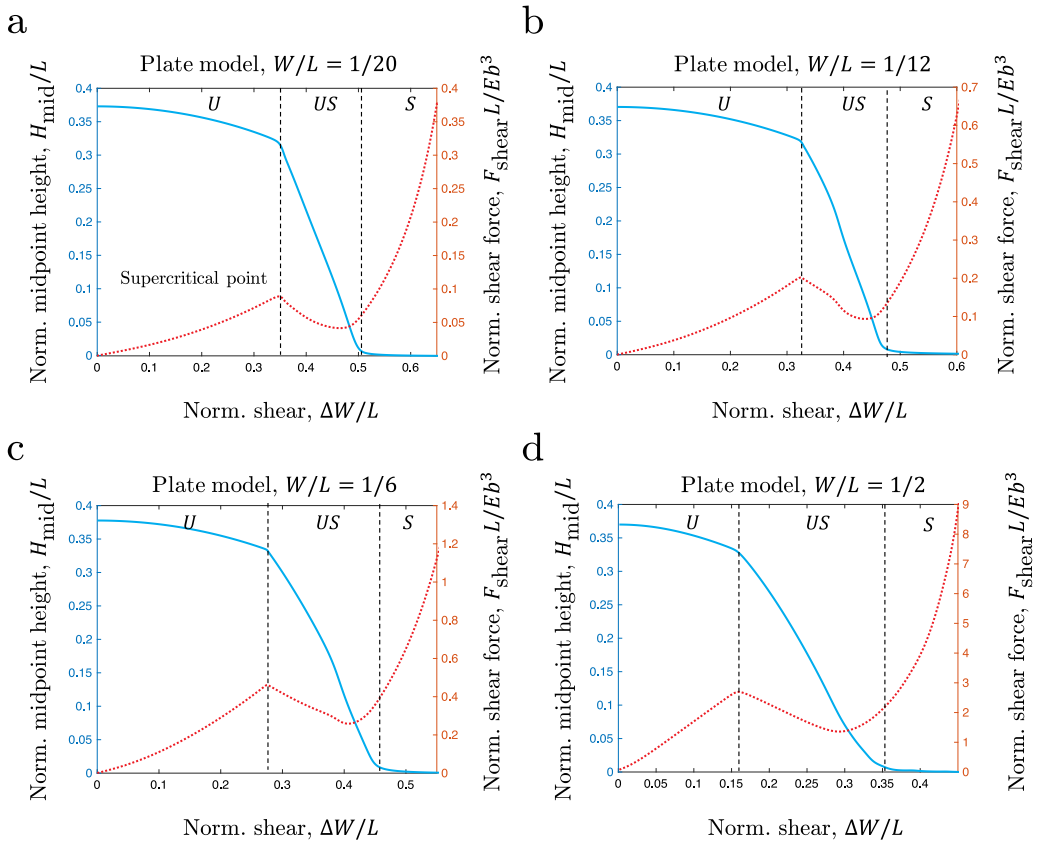

Fig. E.18. Normalized midpoint height, H_{mid}/L (solid line), as well as normalized external shear forces, $F_{\text{shear}}L/Eb^3$ (dashed line), as functions of normalized transverse shear, $\Delta W/L$, for plates with different width, $W/L \in \{1/20, 1/12, 1/6, 1/2\}$. Here $\Delta L/L = 1/2$.

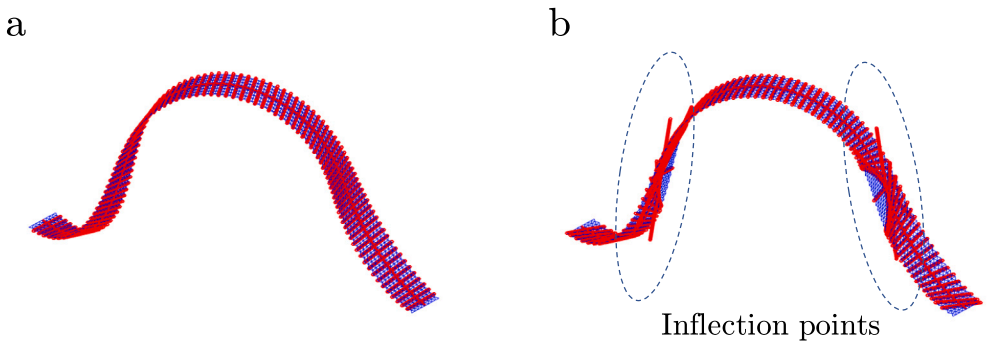

Fig. F.19. (a) Rod-based rendering and (b) ribbon-based rendering from plate centerline data.

Appendix B. Maximum shear

The shearing process tends towards limiting states, past which the sheet cannot deform without stretching somewhere (Yu and Hanna, 2019). In Fig. B.15(a), we show folded strip model to represent a limiting *S*-like pattern, where the red dashed line indicates the incipient conical singularities forming near the clamps, the corresponding deformed configurations from experiment and simulation are in Fig. B.15(b). In the limit, these cones share a single straight line generator formed from a plate diagonal that sets the limiting shear to (Yu and Hanna, 2019)

$$\Delta W_{\max} = \sqrt{L^2 + W^2 - (L - \Delta L)^2} - W. \tag{B.1}$$

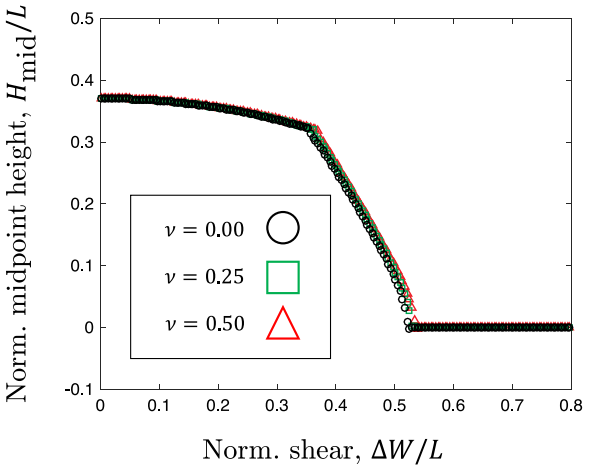

Fig. G.20. Effect of Poisson ratio in anisotropic rod simulation.

Appendix C. Convergence study

Our discrete models show good convergence with space discretization, i.e. number of nodes. In Fig. C.16(a), we plot the normalized height of strip midpoint as a function of normalized transverse displacement for discrete anisotropic rod model; the final results remain unchanged as the number of nodes, M, varies from 50 to 200. We show a similar plot in Fig. C.16(b) to demonstrate that the mechanical response of elastic plate ($\Delta L/L = 1/2$, $W/L = 1/6$) remains unchanged when the mesh number N_{mesh} in DEP varies from 896 to 3596. As we are focusing on the quasistatic response of elastic structures, we omit the convergence with time discretization here.

Appendix D. Bifurcations in US and S patterns

We found bifurcation phenomena when the strip translations from U to US configuration in both experiment and simulation side. After the supercritical pitchfork point, $\Delta W_1/L$, the unstable U configuration would transfer into two symmetric US patterns: $US+$ and $US-$. One can easily switch to another with a small transverse perturbation. Note that the $US+$ and $US-$ are mirror symmetric, e.g. $US-$ pattern is the same as $US+$ looked at from the other side. As the transverse shear increases, $US+$ would translation to $S+$ pattern, and the same is true for $US-$ and $S-$ configurations, as shown in Fig. D.17.

Appendix E. First critical point

In this Appendix, we demonstrate the finding of the supercritical pitchfork from U pattern to US configuration. The first critical point may not be obvious in Fig. 6. Here, in Fig. E.18, we present the normalized external shear force, $F_{\text{shear}}L/Eb^3$, as a function of the normalized transverse displacement, $\Delta W/L$, for the case $\Delta L/L = 1/2$. The external shear forces are computed from the statement of force balance at constrained nodes. We can clearly find the critical point in the load–displacement curves. In the experimental study, the supercritical pitchfork point is the point where bifurcation happens. We applied a small perturbation to the strip to see whether it transitions from one equilibrium to another, e.g. from $US+$ to $US-$. If it remains stable and goes back to the configuration before perturbation, we define this configuration to be still under U phase. The threshold that bifurcation appears is denoted as supercritical pitchfork point in experimental study. The translations from US patterns to S patterns, on the other hand, can be easily obtained from observations on the midpoint height in numerical simulations and experiments. Beyond this critical point, the midpoint height remains unchanged even when transverse shear, ΔW, increases.

Appendix F. Rod-based and ribbon-based kinematics

In this Appendix, we present an anecdote on the kinematics of the rod model and the ribbon model. First, we run the plate simulation and obtain the deformed configuration of the structure. Next, the data is fitted to reconstruct the structure using a centerline-based representation. Towards that end, the nodal positions of the plate centerline (the tangent vectors $\bar{\mathbf{t}}$) as well as the surface normal vectors of the plate centerline (the first material directors $\bar{\mathbf{m}}_1$) are extracted from the simulation. The second material directors can then be easily computed from $\bar{\mathbf{m}}_2 = \bar{\mathbf{t}} \times \bar{\mathbf{m}}_1$. In rod-based models, the edge node based on centerline fitting is

$$\mathbf{x}_{\text{edge}}^{\text{rod}} = \mathbf{x}_{\text{center}} + \frac{W}{2}\bar{\mathbf{m}}_2. \tag{F.1}$$

Fig. F.19(a) shows the centerline and the second material director ($\bar{\mathbf{m}}_2$) from a rod-based representation and we notice that the rod model-based fitted surface closely matches the plate simulation data.

We redo the same exercise using a ribbon-model based representation. Upon computing the centerline curvatures ($\kappa^{(2)}$ and τ) the material frame (Bergou et al., 2010), the ribbon-based edge node is

$$\mathbf{x}_{\text{edge}}^{\text{ribbon}} = \mathbf{x}_{\text{center}} + \frac{W}{2}(\eta\bar{\mathbf{t}} + \bar{\mathbf{m}}_2), \tag{F.2}$$

where $\eta = \tau/\kappa^{(2)}$ is a function of arclength. In Fig. F.19(b), note that this edge location at the inflection points does not match the reliable plate simulation.

Appendix G. Effect of Poisson ratio

We demonstrate the effect of Poisson ratio on the anisotropic rod model is negligible (Yu and Hanna, 2019; Sano and Wada, 2019). In Fig. G.20, we plot the normalized midpoint height as a function of normalized transverse shear with a pre-stressed distance, $\Delta L/L = 1/2$, from the anisotropic rod model. We find negligible variation as Poisson ratio changes from 0.0 to 0.5. In the current study, we used $\nu = 0.0$.

References

Ameline, O., Haliyo, S., Huang, X., Cognet, J.A., 2017. Classifications of ideal 3D elastica shapes at equilibrium. J. Math. Phys. 58 (6), 062902.

Antman, S.S., Jordan, K.B., 1975. 5.—Qualitative aspects of the spatial deformation of non-linearly elastic rods. §. Proc. Roy. Soc. Edinburgh Sect. A 73, 85–105.

Antman, S.S., Kenney, C.S., 1981. Large buckled states of nonlinearly elastic rods under torsion, thrust, and gravity. Arch. Ration. Mech. Anal. 76 (4), 289–338.

Armon, S., Aharoni, H., Moshe, M., Sharon, E., 2014. Shape selection in chiral ribbons: from seed pods to supramolecular assemblies. Soft Matter 10 (16), 2733–2740.

Audoly, B., Clauvelin, N., Brun, P.-T., Bergou, M., Grinspun, E., Wardetzky, M., 2013. A discrete geometric approach for simulating the dynamics of thin viscous threads. J. Comput. Phys. 253, 18–49.

Audoly, B., Neukirch, S., 2005. Fragmentation of rods by cascading cracks: why spaghetti does not break in half. Phys. Rev. Lett. 95 (9), 095505.

Audoly, B., Pomeau, Y., 2010. Elasticity and Geometry: From Hair Curls to the Non-Linear Response of Shells. Oxford University Press.

Audoly, B., Seffen, K.A., 2016. Buckling of naturally curved elastic strips: the ribbon model makes a difference. In: The Mechanics of Ribbons and MÖbius Bands. Springer, pp. 293–320.

Baek, C., Reis, P.M., 2019. Rigidity of hemispherical elastic gridshells under point load indentation. J. Mech. Phys. Solids 124, 411–426.

Baek, C., Sageman-Furnas, A.O., Jawed, M.K., Reis, P.M., 2018. Form finding in elastic gridshells. Proc. Natl. Acad. Sci. 115 (1), 75–80.

Baraff, D., Witkin, A., 1998. Large steps in cloth simulation. In: Proceedings of the 25th Annual Conference on Computer Graphics and Interactive Techniques. ACM, pp. 43–54.

Batty, C., Uribe, A., Audoly, B., Grinspun, E., 2012. Discrete viscous sheets. ACM Trans. Graph. 31 (4), 113.

Bende, N.P., Evans, A.A., Innes-Gold, S., Marin, L.A., Cohen, I., Hayward, R.C., Santangelo, C.D., 2015. Geometrically controlled snapping transitions in shells with curved creases. Proc. Natl. Acad. Sci. 112 (36), 11175–11180.

Bergou, M., Audoly, B., Vouga, E., Wardetzky, M., Grinspun, E., 2010. Discrete viscous threads. ACM Trans. Graph. 29 (4), 116.

Bergou, M., Wardetzky, M., Robinson, S., Audoly, B., Grinspun, E., 2008. Discrete elastic rods. ACM Trans. Graph. 27 (3), 63.

Bonet, J., Wood, R.D., 1997. Nonlinear Continuum Mechanics for Finite Element Analysis. Cambridge university press.

Bridson, R., Marino, S., Fedkiw, R., 2005. Simulation of clothing with folds and wrinkles. In: ACM SIGGRAPH 2005 Courses. ACM, p. 3.

Charrondière, R., Bertails-Descoubes, F., Neukirch, S., Romero, V., 2020. Numerical modeling of inextensible elastic ribbons with curvature-based elements. Comput. Methods Appl. Mech. Engrg. 364, 112922.

Chen, T., Bilal, O.R., Shea, K., Daraio, C., 2018. Harnessing bistability for directional propulsion of soft, untethered robots. Proc. Natl. Acad. Sci. 115 (22), 5698–5702.

Choi, K.-J., Ko, H.-S., 2005. Research problems in clothing simulation. Comput.-Aided Des. 37 (6), 585–592.

De Borst, R., Crisfield, M.A., Remmers, J.J., Verhoosel, C.V., 2012. Nonlinear Finite Element Analysis of Solids and Structures. John Wiley & Sons.

Dias, M.A., Audoly, B., 2014. A non-linear rod model for folded elastic strips. J. Mech. Phys. Solids 62, 57–80.

Dias, M.A., Audoly, B., 2015. Wunderlich, meet kirchhoff: A general and unified description of elastic ribbons and thin rods. J. Elasticity 119 (1–2), 49–66.

Dias, M.A., Dudte, L.H., Mahadevan, L., Santangelo, C.D., 2012. Geometric mechanics of curved crease origami. Phys. Rev. Lett. 109 (11), 114301.

Evkin, A., Kolesnikov, M., Prikazchikov, D.A., 2017. Buckling of a spherical shell under external pressure and inward concentrated load: asymptotic solution. Math. Mech. Solids 22 (6), 1425–1437.

Forterre, Y., Skotheim, J.M., Dumais, J., Mahadevan, L., 2005. How the venus flytrap snaps. Nature 433 (7024), 421.

Ghafouri, R., Bruinsma, R., 2005. Helicoid to spiral ribbon transition. Phys. Rev. Lett. 94 (13), 138101.

Giomi, L., Mahadevan, L., 2010. Statistical mechanics of developable ribbons. Phys. Rev. Lett. 104 (23), 238104.

Gomez, M., Moulton, D.E., Vella, D., 2017. Critical slowing down in purely elastic 'snap-through'instabilities. Nat. Phys. 13 (2), 142.

Goyal, S., Perkins, N.C., Lee, C.L., 2005. Nonlinear dynamics and loop formation in kirchhoff rods with implications to the mechanics of DNA and cables. J. Comput. Phys. 209 (1), 371–389.

Grégoire, M., Schömer, E., 2007. Interactive simulation of one-dimensional flexible parts. Comput. Aided Des. 39 (8), 694–707.

Grinspun, E., Hirani, A.N., Desbrun, M., Schröder, P., 2003. Discrete shells. In: Proceedings of the 2003 ACM SIGGRAPH/Eurographics Symposium on Computer Animation. Eurographics Association, pp. 62–67.

Grinspun, E., Krysl, P., Schröder, P., 2002. CHARMS: a simple framework for adaptive simulation. ACM Trans. Graph. (TOG) 21 (3), 281–290.

Guo, Q., Mehta, A.K., Grover, M.A., Chen, W., Lynn, D.G., Chen, Z., 2014. Shape selection and multi-stability in helical ribbons. Appl. Phys. Lett. 104 (21), 211901.

Heisser, R.H., Patil, V.P., Stoop, N., Villermaux, E., Dunkel, J., 2018. Controlling fracture cascades through twisting and quenching. Proc. Natl. Acad. Sci. 115 (35), 8665–8670.

House, D., Breen, D., 2000. Cloth Modeling and Animation. CRC Press.

Huang, N.-C., 1964. Unsymmetrical buckling of thin shallow spherical shells. J. Appl. Mech. 31 (3), 447–457.

Huang, N.C., 1969. Axisymmetric dynamic snap-through of elastic clamped shallow spherical shells. AIAA J. 7 (2), 215–220.

Huang, W., Jawed, M.K., 2019. Newmark-beta method in discrete elastic rods algorithm to avoid energy dissipation. J. Appl. Mech. 86 (8), 084501.

Hughes, T.J., 2012. The Finite Element Method: Linear Static and Dynamic Finite Element Analysis. Courier Corporation.
Hutchinson, J.W., Thompson, J.T., 2018. Imperfections and energy barriers in shell buckling. Int. J. Solids Struct. 148, 157–168.
Jawed, M.K., Da, F., Joo, J., Grinspun, E., Reis, P.M., 2014. Coiling of elastic rods on rigid substrates. Proc. Natl. Acad. Sci. 111 (41), 14663–14668.
Jawed, M., Novelia, A., O'Reilly, O.M., 2018. A Primer on the Kinematics of Discrete Elastic Rods. Springer.
Ji, W., Waas, A.M., 2008. Dynamic bifurcation buckling of an impacted column. Internat. J. Engrg. Sci. 46 (10), 958–967.
Jiang, X., Pezzulla, M., Shao, H., Ghosh, T.K., Holmes, D.P., 2018. Snapping of bistable, prestressed cylindrical shells. Europhys. Lett. 122 (6), 64003.
Kebadze, E., Guest, S., Pellegrino, S., 2004. Bistable prestressed shell structures. Int. J. Solids Struct. 41 (11–12), 2801–2820.
Kehrbaum, S., Maddocks, J., 1999. Elastic rods, rigid bodies, quaternions and the last quadrature. In: Localization and Solitary Waves in Solid Mechanics. World Scientific, pp. 181–200.
Kleiman, D.M., Hinz, D.F., Takato, Y., Fried, E., 2016. Influence of material stretchability on the equilibrium shape of a Möbius band. Soft Matter 12 (16), 3750–3759.
Lavrenčič, M., Brank, B., 2018. Simulation of shell buckling by implicit dynamics and numerically dissipative schemes. Thin-Walled Struct. 132, 682–699.
Lazarus, A., Florijn, H., Reis, P.M., 2012. Geometry-induced rigidity in nonspherical pressurized elastic shells. Phys. Rev. Lett. 109 (14), 144301.
Lazarus, A., Miller, J., Reis, P.M., 2013. Continuation of equilibria and stability of slender elastic rods using an asymptotic numerical method. J. Mech. Phys. Solids 61 (8), 1712–1736.
Lestringant, C., Audoly, B., Kochmann, D.M., 2019. A discrete, geometrically exact method for simulating nonlinear, elastic and inelastic beams. Comput. Methods Appl. Mech. Engrg. 112741.
Li, X., Huang, W., Jawed, M., 2019. A discrete differential geometry-based approach to numerical simulation of timoshenko beam. Extreme Mech. Lett. 100622.
Li, X., Huang, W., Jawed, M., 2020. Discrete elasto-plastic rods. Extreme Mech. Lett. 100767.
Liang, H., Mahadevan, L., 2009. The shape of a long leaf. Proc. Natl. Acad. Sci. 106 (52), 22049–22054.
Liu, Y., Wang, X., Xu, Y., Xue, Z., Zhang, Y., Ning, X., Cheng, X., Xue, Y., Lu, D., Zhang, Q., et al., 2019. Harnessing the interface mechanics of hard films and soft substrates for 3D assembly by controlled buckling. Proc. Natl. Acad. Sci. 116 (31), 15368–15377.
Marthelot, J., López Jiménez, F., Lee, A., Hutchinson, J.W., Reis, P.M., 2017. Buckling of a pressurized hemispherical shell subjected to a probing force. J. Appl. Mech. 84 (12).
Moore, A., Healey, T.J., 2015. Computation of Unconstrained Elastic Equilibria of Complete Möbius Bands and their Stability. arXiv preprint arXiv:1509.00147.
Morigaki, Y., Wada, H., Tanaka, Y., 2016. Stretching an elastic loop: Crease, helicoid, and pop out. Phys. Rev. Lett. 117 (19), 198003.
Nizette, M., Goriely, A., 1999. Towards a classification of Euler–Kirchhoff filaments. J. Math. Phys. 40 (6), 2830–2866.
Pandey, A., Moulton, D.E., Vella, D., Holmes, D.P., 2014. Dynamics of snapping beams and jumping poppers. Europhys. Lett. 105 (2), 24001.
Panetta, J., Konaković-Luković, M., Isvoranu, F., Bouleau, E., Pauly, M., 2019. X-shells: A new class of deployable beam structures. ACM Trans. Graph. 38 (4), 83.
Pérez, J., Thomaszewski, B., Coros, S., Bickel, B., Canabal, J.A., Sumner, R., Otaduy, M.A., 2015. Design and fabrication of flexible rod meshes. ACM Trans. Graph. 34 (4), 138.
Pezzulla, M., Stoop, N., Jiang, X., Holmes, D.P., 2017. Curvature-driven morphing of non-Euclidean shells. Proc. R. Soc. Lond. Ser. A Math. Phys. Eng. Sci. 473 (2201), 20170087.
Qin, L., Huang, W., Du, Y., Zheng, L., Jawed, M.K., 2020. Genetic algorithm-based inverse design of elastic gridshells. Struct. Multidiscip. Optim. 1–17.
Sadowsky, M., 1930. Ein elementarer Beweis für die Existenz eines abwickelbaren Möbiusschen Bandes und Zurückführung des geometrischen Problems auf ein Variationsproblem.
Sano, T.G., Wada, H., 2018. Snap-buckling in asymmetrically constrained elastic strips. Phys. Rev. E 97 (1), 013002.
Sano, T.G., Wada, H., 2019. Twist-induced snapping in a bent elastic rod and ribbon. Phys. Rev. Lett. 122 (11), 114301.
Savin, T., Kurpios, N.A., Shyer, A.E., Florescu, P., Liang, H., Mahadevan, L., Tabin, C.J., 2011. On the growth and form of the gut. Nature 476 (7358), 57.
Seung, H.S., Nelson, D.R., 1988. Defects in flexible membranes with crystalline order. Phys. Rev. A 38 (2), 1005.
Shen, Z., Huang, J., Chen, W., Bao, H., 2015. Geometrically exact simulation of inextensible ribbon. Comput. Graph. Forum 34 (7), 145–154.
Shim, J., Perdigou, C., Chen, E.R., Bertoldi, K., Reis, P.M., 2012. Buckling-induced encapsulation of structured elastic shells under pressure. Proc. Natl. Acad. Sci. 109 (16), 5978–5983.
Spillmann, J., Teschner, M., 2008a. An adaptive contact model for the robust simulation of knots. Comput. Graph. Forum 27 (2), 497–506.
Spillmann, J., Teschner, M., 2008b. Cosserat nets. IEEE Trans. Vis. Comput. Graphics 15 (2), 325–338.
Starostin, E., van der Heijden, G., 2008. Tension-induced multistability in inextensible helical ribbons. Phys. Rev. Lett. 101 (8), 084301.
Starostin, E., van der Heijden, G., 2015. Equilibrium shapes with stress localisation for inextensible elastic Möbius and other strips. J. Elasticity 119 (1–2), 67–112.
Starostin, E., Van Der Heijden, G., 2007. The shape of a Möbius strip. Nature Mater. 6 (8), 563.
Van der Heijden, G., Neukirch, S., Goss, V., Thompson, J., 2003. Instability and self-contact phenomena in the writhing of clamped rods. Int. J. Mech. Sci. 45 (1), 161–196.
Van der Heijden, G., Thompson, J., 1998. Lock-on to tape-like behaviour in the torsional buckling of anisotropic rods. Physica D 112 (1–2), 201–224.
Van der Heijden, G., Thompson, J., 2000. Helical and localised buckling in twisted rods: a unified analysis of the symmetric case. Nonlinear Dynam. 21 (1), 71–99.
Vandenberghe, N., Villermaux, E., 2013. Geometry and fragmentation of soft brittle impacted bodies. Soft Matter 9 (34), 8162–8176.
Wan, G., Liu, Y., Xu, Z., Jin, C., Dong, L., Han, X., Zhang, J.X., Chen, Z., 2019. Tunable bistability of a clamped elastic beam. Extreme Mech. Lett. 100603.
Wardetzky, M., Bergou, M., Harmon, D., Zorin, D., Grinspun, E., 2007. Discrete quadratic curvature energies. Comput. Aided Geom. Design 24 (8–9), 499–518.
Wood, R.D., Zienkiewicz, O., 1977. Geometrically nonlinear finite element analysis of beams, frames, arches and axisymmetric shells. Comput. Struct. 7 (6), 725–735.
Wunderlich, W., 1962. Über ein abwickelbares Möbiusband. Monatsh. Math. 66 (3), 276–289.
Xu, Z., Fan, Z., Fu, H., Liu, Y., Zi, Y., Huang, Y., Zhang, Y., 2019. Optimization-based approach for the inverse design of ribbon-shaped three-dimensional structures assembled through compressive buckling. Phys. Rev. A 11 (5), 054053.
Yu, T., Hanna, J., 2019. Bifurcations of buckled, clamped anisotropic rods and thin bands under lateral end translations. J. Mech. Phys. Solids 122, 657–685.
Zhang, Y., Jiao, Y., Wu, J., Ma, Y., Feng, X., 2019. Configurations evolution of a buckled ribbon in response to out-of-plane loading. Extreme Mech. Lett. 100604.
Zienkiewicz, O.C., Taylor, R.L., 2005. The Finite Element Method for Solid and Structural Mechanics. Elsevier.